Friction https://mc03.manuscriptcentral.com/friction
https://doi.org/10.26599/FRICT.2026.9441228

Research Article

A NURBS-based isogeometric analysis model for soft EHL contacts

Yan Tong✉, Michael Müller✉

Institute for Acoustics and Dynamics, Technische Universität Braunschweig, Langer Kamp 19, 38106 Braunschweig, Lower Saxony, Germany

✉ Corresponding author. E-mail: y.tong@tu-braunschweig.de (Yan Tong), mi.mueller@tu-bs.de (Michael Müller)

Received: June 24, 2025; Revised: January 2, 2026; Accepted: January 27, 2026

Abstract: This paper presents a NURBS-based isogeometric analysis framework for modeling both hard and soft elastohydrodynamic lubrication (EHL) contacts under the fully flooded condition. Unlike conventional approaches, the framework incorporates nonlinear solid deformation within a unified weak formulation and employs a mortar method to flexibly couple the fluid and solid domains with independent discretizations. Benchmark tests show excellent agreement with reference ANSYS FSI simulations while reducing the computational time by about 99% for both hard and soft EHL line contacts. The framework is further applied to a soft EHL point contact between a

hyperelastic hemisphere and a rigid plane, confirming that nonlinear solid deformation strongly affects the film thickness and frictional response. Finally, the influence of surface roughness is investigated, revealing that transversely oriented topographies yield superior lubrication performance, as indicated by a higher transition load and a lower friction coefficient.

Keywords: Cavitation, Mortar method, Fluid-structure-interaction, Topography orientations

1 Introduction

In machine elements involving lubrication, such as bearings and gears, solid contact surfaces are typically separated by a thin film of lubricant to reduce friction and wear. When the hydrodynamic pressure transmitted by the lubricant is sufficiently high, significant elastic deformations of the contact surfaces can occur, thereby altering the film thickness. This regime is known as elastohydrodynamically lubricated (EHL) contacts, which has gained substantial interest in establishing appropriate and efficient numerical models over the past decades. The EHL problem is inherently multi-physical due to the fluid-structure interaction (FSI) between lubricant hydrodynamics and solid deformations. Generally, it can be categorized into two types, "hard" and "soft", based on the rigidity of the solid materials.

Early numerical models focused primarily on the traditional hard EHL problem, where solids possess a high elastic modulus and their deformations are treated as linear elastic. Additionally, the high-pressure area is small compared to the size of the solid bodies, allowing for the approximation of deformations using the Boussinesq function (derived from the half-space theory [18]). The Reynolds equation is employed to represent the viscous lubricant flow within the narrow gap, but it must be combined with appropriate boundary conditions to account for cavitation phenomena (for more details refer to Braun and Hannon [5]). Moreover, it is crucial to incorporate equations describing the lubricant's rheological behavior, as Lugt and Morales-Espejel [23] indicate that the

fluid pressure can reach 1 to 3 GPa, which significantly affects the viscosity (piezo-viscous effect) and density of the lubricant.

The Boussinesq equation, Reynolds equation, and rheological law constitute a highly nonlinear system for the hard EHL problem. In the seminal work of Hamrock and Dowson [10], the system of equations was discretized using the finite difference method (FDM) for its simplicity and solved using the relaxation method. Despite accurately predicting the deformed film thickness, their model exhibited convergence problems due to the weak fluid-structure coupling. Specifically, they solved the equations governing the flow and structural deformations sequentially until converged solutions were achieved for both parts. This method results in reduced robustness, particularly for highly loaded EHL contacts, since the information transfer between the fluid and the structure is one-way rather than simultaneous.

Lubrecht et al. [22] optimized Hamrock and Dowson's model using a multigrid approach, improving both computation speed and convergence efficiency for solving the Reynolds equation with fine meshes. Later, Venner [42] introduced a multilevel multi-integration (MLMI) method for evaluating solid deformations in fine meshes, greatly accelerating the computational process. An alternative to MLMI for efficient deformation calculations is the discrete convolution and fast Fourier transform (DC-FFT) method [17, 19].

In recent decades, several works (e.g. Hsiao et al. [14], Holmes et al. [13]) have focused on developing EHL models using strong coupling (also known as monolithic coupling), whereby the equations for fluid and solid parts were solved simultaneously. This strategy led to valid solutions within a few iterations, illustrating its extremely rapid convergence speed. However, structural deformations were still computed using the Boussinesq approximation (or its differential form), leading to a dense Jacobian matrix and significant computational expense. Moreover, their pressure solutions exhibited unphysical oscillations, especially under heavy loads.

Habchi et al. [9] replaced the Boussinesq equation with a simplified momentum balance equation. The equations were then discretized using the finite element method (FEM), resulting in a sparse Jacobian matrix since each element node is only associated with nodes within the same element. They also employed the Streamline upwind Petrov–Galerkin (SUPG, proposed by Brooks and Hughes [6]) and Galerkin least-squares (GLS, proposed by Hughes et al. [16]) methods to stabilize their formulations and eliminate pressure oscillations.

Notably, all the models mentioned above utilized the Swift-Stieber condition (see Braun and Hannon [5] for a detailed description) to incorporate the pressure variation caused by the cavitation phenomena. Despite being widely applied, this cavitation condition cannot ensure mass conservation of the lubricant. Another limitation of these models is their assumption of linear elasticity, which is invalid for soft EHL problems. In such scenarios, materials with a low elastic modulus exhibit highly nonlinear behavior, as can be observed in rubber seals or biological systems like knee and hip joints. Unlike the hard EHL problem, the soft EHL problem typically involves large structural deformations despite low hydrodynamic pressure, leading to increased modeling challenges.

In this context, Hansen et al. [12] proposed the EHL-FBNS model based on the finite volume method, which enables unsteady simulations with a mass-conserving cavitation treatment following the Jakobsson-Floberg-Olsson (JFO) theory [5]. While this represents an important improvement on the fluid side, their approach still relies on the half-space method for solid deformation and therefore cannot be extended to soft EHL contact problems.

Stupkiewicz et al. [32] developed a FEM-based model that primarily addresses soft EHL problems. They solved large structural deformations as a subproblem through the momentum balance equation and incorporated the JFO condition for cavitation. However, the fluid domain in this model is defined on one of the contact surfaces, which strictly constrains its geometry and mesh size. In addition, it only considers steady-state conditions, limiting its ability to capture the transient evolution of the mixture flow.

Faraji et al. [8] extended the model of Stupkiewicz et al. [32] by incorporating the effects of surface roughness in a stochastic manner via the averaged Reynolds equation. A disadvantage of this approach is that it does not account for the direct interaction between the roughness and the fluid, which is a significant factor in the soft EHL regime. To the best of our knowledge, no deterministic model currently exists that can compute both the local transient fluid flow and the changes in surface topography in soft EHL contacts between rough surfaces.

The present work develops a model capable of dealing with both hard and soft EHL problems under the isogeometric analysis (IGA) framework. Compared to the conventional FEM, IGA applies the same basis functions to model the geometry and construct the solution space, so that no extra meshing process is required. The most widely used basis functions in IGA are non-uniform rational B-splines (NURBS), which extend B-splines to permit exact representations of all conic sections and are convenient for free-form surface constructions. The benefits of NURBS in improving continuity and its potential for FSI modeling were already suggested in the foundational works by Hughes et al. [15]. Therefore, they will not be discussed further here to avoid repetition.

This study emphasizes the formulation and validation of the proposed NURBS-based EHL framework under the fully flooded condition, where the lubricant supply is sufficient. The framework incorporates nonlinear finite-strain hyperelasticity and is benchmarked against ANSYS for both hard and soft EHL contacts, providing new insights into deformation behavior and cavitation development, including the influence of surface texture orientations. By contrast, a complementary study has applied the same framework to soft EHL contacts under the starved condition, a different physical regime in which insufficient lubricant supply governs the response, with emphasis on how starvation alters film thickness and frictional behavior [36].

The paper is structured as follows: Section 2 details the governing equations for EHL contacts that account for nonlinear large deformations, along with the corresponding weak formulations. In Section 3, these formulations are discretized within the NURBS-based IGA framework, and a

mortar-based coupling formulation is developed. Section 4 presents benchmark tests for EHL line contacts using the newly developed model. In Section 5, the model is applied to study the central film thickness and frictional behavior in a soft EHL point contact problem. Section 6 investigates the influence of topography orientation on the COF in soft EHL contacts considering surface roughness. Finally, the main conclusions are summarized in Section 7.

2 EHL model considering large deformation and cavitation

This section presents the mathematical description for EHL problems within the new model. It involves two elastic bodies undergoing contact, denoted as $\mathcal{B}^i$ $(i = 1, 2)$. A layer of lubricant is introduced between them to separate the contact surfaces and transmit forces (see Fig. 1).

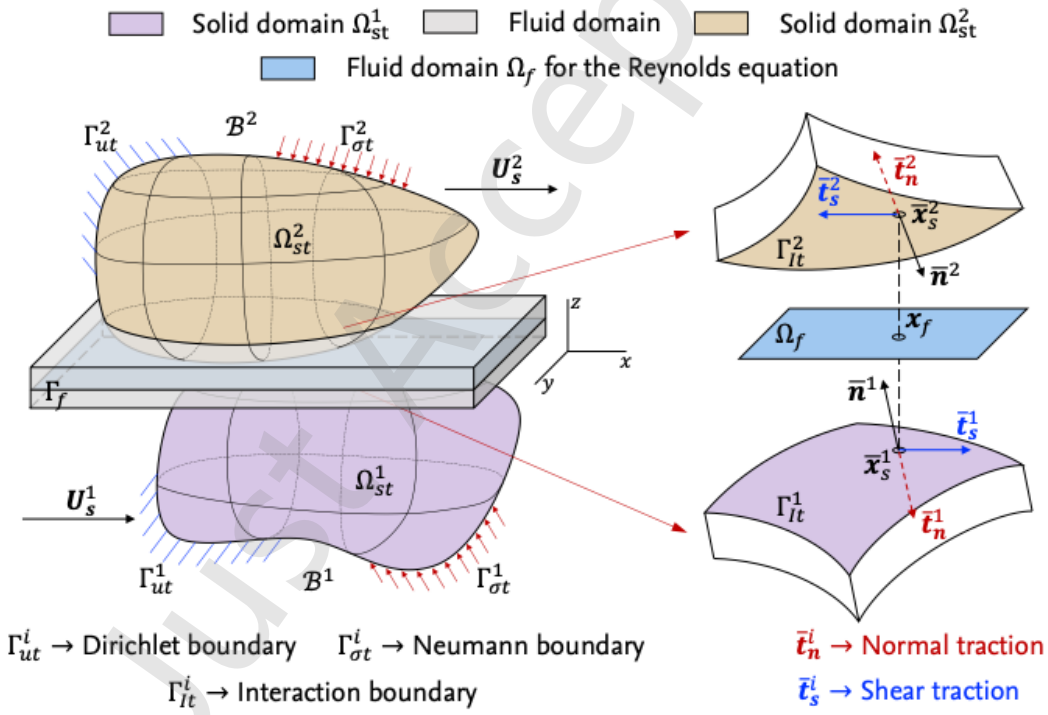

Fig. 1 Schematic representation of the EHL contact between two elastic bodies, showing the coupled configuration of the fluid and solid domains with their corresponding boundaries (left), and the vertical projection of a fluid point onto the interaction boundaries used to define the film thickness, together with the notation for the normal and shear tractions (right).

Solid $\mathcal{B}^i$ is assumed to move at a constant velocity $\boldsymbol{U}^i_s$. It occupies the bounded domain $\Omega^i_{st} \subset R^3$, where the subscript t indicates the current time. The boundary of domain Ω^i_{st} can be divided into

three parts: Γ_{ut}^i with prescribed displacement (Dirichlet boundary), $\Gamma_{\sigma t}^i$ with prescribed surface loads (Neumann boundary), and Γ_{lt}^i, where interactions between the solid body and fluid take place.

Typically, a reference configuration Ω_{s0}^i is chosen at the initial time $t_0 = 0$ to take finite deformations into account. The coordinate vector of a material point in the current configuration ($\boldsymbol{x}_s^i \in \Omega_{st}^i$) is related to its counterpart in the reference configuration ($\boldsymbol{X}_s^i \in \Omega_{s0}^i$) through the Lagrangian description

$$\boldsymbol{x}_s^i = \boldsymbol{\varphi}^i(\boldsymbol{X}_s^i, t) = \boldsymbol{\varphi}_t^i(\boldsymbol{X}_s^i) = \boldsymbol{X}_s^i + \boldsymbol{u}_s^i, \tag{1}$$

where $\boldsymbol{\varphi}_t^i$ is a bijective mapping from domain Ω_{s0}^i to Ω_{st}^i, and $\boldsymbol{u}_s^i$ measures the displacement.

As mentioned in Sec. 1, starved lubrication or reduction in hydrodynamic pressure can lead to the formation of cavitation bubbles. In tribological studies, the mixture flow of lubricant and bubbles is described using the Reynolds equation, given its low-Reynolds-number characteristic within the narrow gap between contact surfaces (see the handbook by Bartel [3]).

The Reynolds equation is derived by averaging the mass-continuity equation over the gap height direction. This direction could be defined differently based on the specific scenario (see Temizer and Stupkiewicz [33]). In the following, the curvature effects of contact surfaces are neglected for simplicity, and the z-direction is chosen as the gap height direction. As a result, the three-dimensional fluid domain (the grey part in Fig. 1) is reduced to a surface domain Ω_f (the blue part in Fig. 1, orthogonal to the z-axis).

In this work, Ω_f is fixed in position and does not move over time. Certainly, the model can be extended to account for a movable fluid domain using the arbitrary Lagrangian-Eulerian (ALE) method. The specific numerical implementation of this extension was documented by Tong et al. [39], and will not be discussed further here.

2.1 Mixture flow of lubricant and cavitation

To establish the mapping between the fluid and solid sides, it is assumed that the interaction boundary Γ_{lt}^i is smooth with $\mathcal{C}^2$-continuity and can be parameterized by the convective coordinates

$\boldsymbol{\xi}_{sI}^{i} = \left(\xi_{sI}^{i1}, \xi_{sI}^{i2}\right)$. For a given point $\boldsymbol{x}_f \in \Omega_f$, its projection onto the interaction boundary Γ_{It}^{i} can be denoted as $\boldsymbol{x}_s^i\left(\bar{\boldsymbol{\xi}}_{sI}^{i}\right)$, with $\bar{\boldsymbol{\xi}}_{sI}^{i} = \left(\bar{\xi}_{sI}^{i1}, \bar{\xi}_{sI}^{i2}\right)$ representing the convective coordinates of the projection point. $\bar{\boldsymbol{\xi}}_{sI}^{i}$ is determined by solving

$$\left[\boldsymbol{x}_f - \boldsymbol{x}_s^i\left(\bar{\boldsymbol{\xi}}_{sI}^{i}\right)\right] \cdot \boldsymbol{e}_1 = \left[\boldsymbol{x}_f - \boldsymbol{x}_s^i\left(\bar{\boldsymbol{\xi}}_{sI}^{i}\right)\right] \cdot \boldsymbol{e}_2 = 0, \tag{2}$$

where $\boldsymbol{e}$ stands for the standard basis vector, and the subscripts $1-3$ indicate the $x-z$ directions. Subsequently, the parameters associated with the projection coordinates $\bar{\boldsymbol{\xi}}_{sI}^{i}$ will be simplified using a bar notation, i.e., $\blacksquare\left(\bar{\boldsymbol{\xi}}_{sI}^{i}\right) \rightarrow \bar{\blacksquare}$. Thus, $\boldsymbol{x}_s^i\left(\bar{\boldsymbol{\xi}}_{sI}^{i}\right)$ will be written as $\bar{\boldsymbol{x}}_s^i$. The gap height h is then measured by the vertical distance between these projection points:

$$h = \left(\bar{\boldsymbol{x}}_s^2 - \bar{\boldsymbol{x}}_s^1\right) \cdot \boldsymbol{e}_3. \tag{3}$$

Accordingly, the averaged mass-continuity equation in Ω_f (for complete derivations see Tong et al. [38]) is written as

$$\frac{\partial}{\partial t}(\bar{\rho}h) + \nabla \cdot (\bar{\rho}\bar{\boldsymbol{u}}h) = 0. \tag{4}$$

Herein, $\bar{\boldsymbol{u}}$ and $\bar{\rho}$ represent the averaged flow velocity over the gap height direction. Given that the flow in z-direction is negligible and viscous forces are dominant for this micro-channel flow (see Bartel [3]), $\bar{\boldsymbol{u}}$ can be calculated through a simplified Navier-Stokes equation:

$$\bar{\boldsymbol{u}} = \bar{\boldsymbol{U}}_s - \frac{h^2}{12\eta}\nabla p. \tag{5}$$

In this equation, $\bar{\boldsymbol{U}}_s = \left(\boldsymbol{U}_s^1 + \boldsymbol{U}_s^2\right)/2$ is the mean velocity of solid bodies, η is the lubricant viscosity, and p denotes the averaged hydrodynamic pressure. Combining Eqs. (4) and (5) results in the Reynolds equation:

$$\frac{\partial}{\partial t}(\bar{\rho}h) + \nabla \cdot (\bar{\rho}\bar{\boldsymbol{U}}_s h) - \nabla \cdot \left(\frac{\bar{\rho}h^3}{12\eta}\nabla p\right) = 0. \tag{6}$$

The fluid domain Ω_f can be divided into two regions depending on the presence of cavitation bubbles: the full-film region Ω_f^+ and the cavitation region Ω_f^-, with the boundary Γ_{cav} separating

them (see Fig. 2). The full-film region is entirely filled with the lubricant, which is assumed to be incompressible with a density of ρ_0. In contrast, the pressure in the cavitation region p_c is considered constant, as observed in numerous experimental studies [5]. These constraints can be expressed as

$$p \geq p_c,\ \bar{\rho} = \rho_0 \text{ in } \Omega_f^+, \text{ and } p = p_c,\ \bar{\rho} \leq \rho_0 \text{ in } \Omega_f^-. \tag{7}$$

Without loss of generality, p_c is set to 0 Pa in this work.

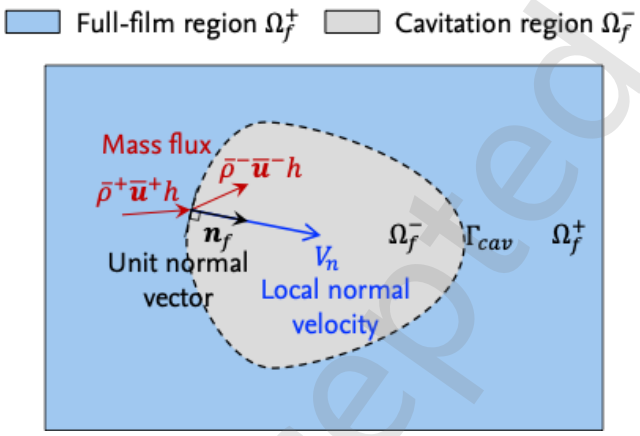

Fig. 2 Top view of the fluid domain Ω_f, showing its subdivision into the full-film region Ω_f^+ and the cavitation region Ω_f^-, separated by the cavitation boundary Γ_{cav}. The difference between the inflow and outflow mass fluxes across Γ_{cav} corresponds to the flux displaced by the moving cavitation boundary with its local normal velocity V_n, ensuring mass-flux continuity.

Notably, the constraints in Eq. (7) can cause a discontinuity of pressure on the cavitation boundary Γ_{cav}, leading to the averaged flow velocity being undefined. In this case, the Reynolds equation (7) is not valid on Γ_{cav}. To ensure the continuity of mass flux $\bar{\rho}\bar{\boldsymbol{u}}h$ on Γ_{cav}, the JFO boundary condition [5] needs to be introduced:

$$(\bar{\rho}^+\bar{\boldsymbol{u}}^+h - \bar{\rho}^-\bar{\boldsymbol{u}}^-h)\cdot\boldsymbol{n}_f = (\bar{\rho}^+ - \bar{\rho}^-)hV_n. \tag{8}$$

The superscripts $+$ and $-$ in Eq. (8) indicate the limit values on Γ_{cav} from the side of Ω^+ and Ω^-, respectively (see Fig. 2). In addition, $\boldsymbol{n}_f$ is the unit normal vector pointing from Ω^+ to Ω^-, and V_n represents the local normal velocity at which Γ_{cav} is moving (not the flow velocity).

In summary, the mixture flow is governed by the Reynolds equation (6) and the cavitation constraints in Eqs. (7) and (8). Tong et al. [38] developed a formulation based on the Augmented Lagrangian (AL) method to deal with the complementarity constraints in Eq. (7).

A new variable, the void fraction $r = 1 - \bar{\rho}/\rho_0$, is introduced to represent the local volume fraction of cavitation bubbles across the film thickness: $r = 0$ denotes a fully filled lubricant region, whereas $r > 0$ indicates a partially filled (cavitated) region. Within the AL framework, r is combined with the pressure p to construct the augmented Lagrangian multiplier $\hat{r} = -r + \epsilon p$, where ϵ is a positively defined penalty parameter. Notably, ϵ influences only the convergence behavior (stability and convergence rate) of the nonlinear iterations, but does not affect the final converged solution for either p or r. Excessively large values may lead to oscillatory or divergent Newton steps, whereas overly small values slow down convergence while remaining robust. Based on preliminary numerical experiments, a value of $\epsilon = 10^{-3}$ is adopted for all simulations presented in this work, where it provides stable and efficient convergence.

The pressure contribution in $\hat{r}$ acts as a regularization term, allowing the AL multiplier to vary smoothly across the full-film and cavitation regions. Based on this definition, a piecewise AL functional l_{cav} can then be constructed as

$$l_{cav}(p, r) = \begin{cases} \left(-r + \frac{\epsilon}{2} p\right) p, & \hat{r} \leq 0 \text{ (cavitation)} \\ -\frac{1}{2\epsilon} r^2, & \hat{r} > 0 \text{ (full film)} \end{cases}. \tag{9}$$

It converts the constraints in Eq. (7) into equation form:

$$\frac{\partial l_{cav}}{\partial r} = 0. \tag{10}$$

Although most existing soft EHL studies employ FDM to solve the Reynolds equation [1, 28, 29], our previous works [35, 38] have already provided a detailed comparison between an FDM-based model and an IGA-based mixture flow model. The results demonstrated that the proposed model achieves higher accuracy with significantly fewer degrees of freedom, while also improving

convergence and reducing computational time. Furthermore, the low continuity of FDM (limited to C^0) tends to introduce distortion in the transfer of fluid quantities to the solid domain, thereby slowing down the coupling convergence.

By contrast, employing a unified IGA framework ensures that the pressure and cavitation volume fraction obtained on the fluid side possess high continuity, which in turn guarantees optimal performance in the coupling with the solid deformation part. Building on these advantages, the present study adopts the proposed IGA-based model to solve the Reynolds equation with cavitation constraints.

In general, the external boundary of the fluid domain, Γ_f, can be subdivided into three distinct parts, namely Γ_{fd}, Γ_{fn}, and Γ_{ff}, corresponding to Dirichlet, Neumann, and free boundaries, respectively:

- On Γ_{fd}, Dirichlet boundary conditions are prescribed for both p and r as

$$p = p_D \text{ and } r = r_D \text{ on } \Gamma_{fd}, \tag{11}$$

  This type of condition is typically applied at the inflow boundary, where the prescribed pressure p_D usually corresponds to the ambient pressure, while the void fraction r_D represents the prevailing lubrication regime. A constant value ($r_D = 0$) characterizes a fully flooded inlet, whereas a nonzero distribution ($r_D > 0$) indicates a starved lubrication state.

- On Γ_{fn}, Neumann boundary conditions are applied, generally corresponding to a prescribed inflow or outflow mass flux. In this case, the normal pressure gradient is specified to represent the imposed flow rate or pressure-driven outflow:

$$\frac{h^3}{12\eta}\nabla p \cdot \boldsymbol{n}_{fn} = \hat{q}_{fn} \text{ on } \Gamma_{fn}. \tag{12}$$

- On Γ_{ff}, free boundary conditions are assumed. This type of condition is typically assigned to the outflow region, where no explicit constraints are imposed on either p or r, allowing

both variables to evolve freely in accordance with the cavitation condition and overall mass conservation.

In accordance with the above boundary specifications, the solution spaces (U_p and U_r) and test function spaces (V_p and V_r) are introduced in the standard sense such that the Dirichlet conditions are properly enforced. The weak formulation for the mixture flow problem is then expressed as

$$\text{Find } p \in U_p \text{ and } r \in U_r, \text{ such that } \forall \delta p \in V_p,\ \delta r \in V_r,$$

$$\delta \Pi_f = \delta \Pi_{rey} + \delta \Pi_{cav} + \int_{\Gamma_{fn}} \delta p\, \hat{q}_{fn}\, \mathrm{d}\Gamma = 0, \text{ with} \tag{13}$$

$$\delta \Pi_{rey} = \int_{\Omega_f} \delta p \frac{\partial[(1-r)h]}{\partial t}\, \mathrm{d}\Omega + \int_{\Omega_f} \frac{h^3}{12\eta} \nabla \delta p \cdot \nabla p\, \mathrm{d}\Omega - \int_{\Omega_f} [(1-r)h] \nabla \delta p \cdot \overline{\boldsymbol{U}}_s\, \mathrm{d}\Omega, \tag{14}$$

$$\delta \Pi_{cav} = \int_{\Omega_f} \delta r \frac{\partial l_{cav}}{\partial r}\, \mathrm{d}\Omega. \tag{15}$$

The derivations as well as the linearization process have been thoroughly documented by Tong et al. [38] and will not be repeated here. They also demonstrated that the discretization within the IGA framework is based on the Galerkin method, enabling the discontinuous pressure distribution on Γ_{cav} to be interpolated and approximated by continuous basis functions. Consequently, the constraint in Eq. (8) is inherently satisfied in the discretized solution spaces without the need for additional consideration.

2.2 Solid deformation

As in most tribological studies, this work does not focus on the acceleration process of the solids but rather explores the frictional behavior under constant relative velocity. The transient effects in solid bodies are therefore negligible compared to those in the fluid within the same time frame. Consequently, solid movement is considered a quasi-static process. For solid $\mathcal{B}^i$, its deformation and stress are governed by the momentum balance equation in the reference configuration Ω_{s0}^i:

$$\mathrm{Div}^i \boldsymbol{P}^i + \rho_0^i \widehat{\boldsymbol{b}}^i = 0. \tag{16}$$

Here, $\boldsymbol{P}^i$ is the first Piola-Kirchhoff stress tensor, ρ_0^i denotes the mass density in the reference configuration, and $\widehat{\boldsymbol{b}}^i$ describes the body force (e.g. gravity).

The boundary conditions for $\mathcal{B}^i$ are given with respect to the reference configuration as

$$\boldsymbol{x}_s^i = \widehat{\boldsymbol{x}}^i \text{ on } \Gamma_{u0}^i, \quad \boldsymbol{T}^i = \boldsymbol{P}^i \cdot \boldsymbol{N}^i = \widehat{\boldsymbol{T}}^i \text{ on } \Gamma_{\sigma 0}^i. \tag{17}$$

$\widehat{\boldsymbol{x}}^i$ represents the constraints on the Dirichlet boundary, and $\widehat{\boldsymbol{T}}^i$ is the prescribed Cauchy traction on the Neumann boundary.

Notably, on the interaction boundary, solid $\mathcal{B}^i$ also experiences an interaction force from the fluid. Considering that the direction and magnitude of this force change with solid deformation and fluid flow, it is evaluated on Γ_{It}^i with respect to the current configuration (see Fig. 1). If the hydrodynamic pressure at $\boldsymbol{x}_f$ is determined to be p, the pressure at the projection point $\overline{\boldsymbol{x}}_s^i$ is also equal to p due to the negligible pressure gradient in the gap height direction (see Bartel [3]). Since the hydrodynamic pressure acts perpendicular to the solid surface, a normal traction $\bar{\boldsymbol{t}}_n^i$ at $\overline{\boldsymbol{x}}_s^i$ can be defined through

$$\bar{\boldsymbol{t}}_n^i = -p\overline{\boldsymbol{n}}^i, \tag{18}$$

where $\overline{\boldsymbol{n}}^i$ denotes the unit normal vector at $\overline{\boldsymbol{x}}_s^i$ in the current configuration.

Additionally, $\overline{\boldsymbol{x}}_s^i$ is subjected to a traction $\bar{\boldsymbol{t}}_s^i$ arising from the fluid shear stress, which is proportional to the shear rate near solid surfaces. Since the flow exhibits a parabolic profile along the gap height direction (detailed explanations are found in Bartel [3]), the shear traction $\bar{\boldsymbol{t}}_s^i$ is given by

$$\bar{\boldsymbol{t}}_s^i = -(-1)^i \frac{\eta}{h} \boldsymbol{U}_{sd} - \frac{h}{2} \nabla p, \tag{19}$$

with $\boldsymbol{U}_{sd} = \boldsymbol{U}_s^2 - \boldsymbol{U}_s^1$ being the velocity difference between contact surfaces. Notably, $\bar{\boldsymbol{t}}_n^i$ and $\bar{\boldsymbol{t}}_s^i$ are unknown a priori and must be implicitly computed during the coupling process.

The weak formulation for $\mathcal{B}^i$ is then expressed as

$$\text{Find } \boldsymbol{x}_s^i \in U_s^i, \text{ such that } \forall \delta \boldsymbol{x}_s^i \in V_s^i,$$

$$\delta \Pi_s^i = \delta \Pi_{s,nc}^i + \delta \Pi_{s,c}^i = 0, \text{ with} \tag{20}$$

$$\delta\Pi_{s,nc}^{i} = \int_{\Omega_{s0}^{i}} \mathrm{Grad}^{i}\,\delta\boldsymbol{x}_{s}^{i} : \boldsymbol{P}^{i}\,\mathrm{d}\Omega - \int_{\Omega_{s0}^{i}} \delta\boldsymbol{x}_{s}^{i}\cdot\rho_{0}^{i}\widehat{\boldsymbol{b}}^{i}\,\mathrm{d}\Omega - \int_{\Gamma_{\sigma 0}^{i}} \delta\boldsymbol{x}_{s}^{i}\cdot\widehat{\boldsymbol{T}}^{i}\,\mathrm{d}\Gamma, \tag{21}$$

$$\delta\Pi_{s,c}^{i} = -\int_{\Gamma_{It}^{i}} \delta\bar{\boldsymbol{x}}_{s}^{i}\cdot\left(\bar{\boldsymbol{t}}_{n}^{i} + \bar{\boldsymbol{t}}_{s}^{i}\right)\mathrm{d}\Gamma. \tag{22}$$

Herein, the solution space U_s^i and the corresponding test space V_s^i follow the conventional variational definitions, as described in the FEM literature (e.g. Wriggers [44]), ensuring that the essential boundary conditions on Γ_{u0}^i are properly satisfied.

$\delta\Pi_s^i$ can also be understood as the sum of the virtual work done on solid $\mathcal{B}^i$. The subscripts c and nc are used to distinguish the terms in $\delta\Pi_s^i$ that involve or do not involve coupling. The process for computing and linearizing the non-coupling term $\delta\Pi_{s,nc}^i$ is standard (refer to Wriggers [44]) and will not be covered in this work. The primary focus is on the treatment of the coupling term $\delta\Pi_{s,c}^i$, which will be explained in Sec. 2.3.

2.3 Virtual work on the interaction interface

Although the counterpart of the coupling term $\delta\Pi_{s,c}^i$ does not appear explicitly in the weak formulation Eq. (13) governing the mixture flow, it is implicitly contained through the pressure–thickness coupling in the fluid domain. Specifically, the virtual pressure field δp in Eq. (13) is energetically conjugate to the film thickness h, which in turn depend on the deformation of the solid surfaces. Hence, any virtual change in h induced by $\delta\bar{\boldsymbol{x}}_s^i$ leads to a corresponding variation in the pressure field. This implicit conjugate relationship allows the coupling term $\delta\Pi_{s,c}^i$ to satisfy the overall virtual work balance and thus maintain energetic consistency between the solid and fluid domains.

The data-flow relationships between the solid and fluid submodels are illustrated in Fig. 3. Each time-step solver couples the solid and fluid solvers through the transfer of deformation from the solids to the fluid domain and the feedback of pressure and tractions from the fluid to the solids. The

red variables denote the unknowns that are solved within each time step, namely the pressure p, the current configuration $\boldsymbol{x}_s^i$ of the solid bodies, and the void fraction r.

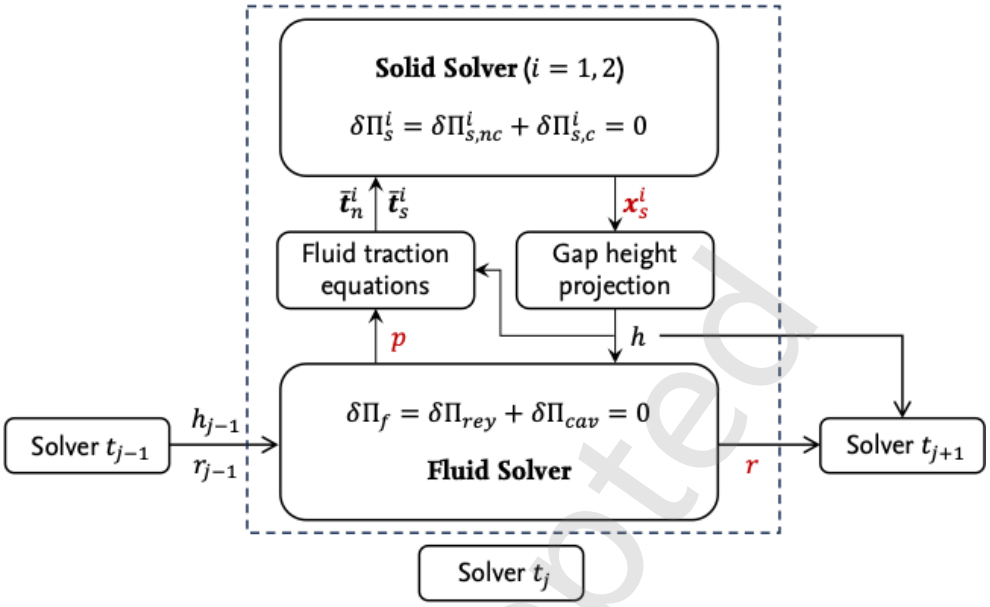

Fig. 3 Data-flow relationships between the fluid and solid submodels of the proposed EHL model. The red variables ($\boldsymbol{x}_s^i$, p, and r) denote the unknowns in each time-step solver. The dashed box indicates the coupled solver at time step t_j, which receives h_{j-1} and r_{j-1} from the previous step and provides the updated h and r for the next step t_{j+1}.

In this model, the weak formulations in Eqs. (13) and (20) are monolithically coupled, implying that all unknowns are solved simultaneously by means of the Newton-Raphson method. Therefore, it is crucial to correctly evaluate the virtual work $\delta\Pi_{s,c}^i$ defined in Eq. (22). By substituting Eqs. (18) and (19) into Eq. (22), $\delta\Pi_{s,c}^i$ can be reformulated as

$$\delta\Pi_{s,c}^i = \int_{\Gamma_{It}^i} \delta\bar{x}_{sn}^i p \, \mathrm{d}\Gamma + (-1)^i \eta \int_{\Gamma_{It}^i} \delta\bar{x}_{ss1}^i \frac{1}{h} \, \mathrm{d}\Gamma + \frac{1}{2} \int_{\Gamma_{It}^i} \delta\bar{x}_{ss2}^i h \, \mathrm{d}\Gamma. \tag{23}$$

Here, $\delta\bar{x}_{sn}^i$, $\delta\bar{x}_{ss1}^i$, and $\delta\bar{x}_{ss2}^i$ denote the auxiliary variations introduced to simplify the representation of the virtual work along the normal and tangential directions. These quantities account for the geometric projection of the fluid-solid interface and maintain the consistency of the interface formulation even under large configuration changes. Their detailed derivations from the surface parameterization and convective coordinate variations are provided in Appendix A.

3 NURBS-based discretization

In the newly developed EHL model, both the fluid and solid subproblems are discretized and solved within the NURBS-based IGA framework. The non-coupling term $\delta\Pi_{s,nc}^{i}$ in the solid formulation, as defined in Eq. (21), follows the same discretization process as in a standard hyperelasticity problem, and will not be derived here (for further details, see Cottrell et al. [7]). Additionally, the discretization for the fluid part (see Eq. (13)) has been comprehensively documented in Tong et al. [38] and will also not be derived here.

Given that the fluid domain Ω_f and the solid interaction boundary Γ_{It}^{i} typically employ non-matching meshes, the virtual work $\delta\Pi_{s,c}^{i}$ defined in Eq. (23) involves quantities that depend on two different sets of basis functions. Therefore, this section focuses on dealing with this specific term using the mortar method. The standard NURBS terminology will be utilized throughout the derivation, with extensive references available in Piegl and Tiller [24].

3.1 Discretization for the fundamental unknowns

The univariate NURBS basis functions are constructed based on a given non-decreasing knot vector

$$\boldsymbol{\Xi} = \{\xi_1, \xi_2, \ \ldots, \xi_m\}. \tag{24}$$

Generally, to achieve the polynomial order of p, the first $p+1$ knots are set equal, as are the last $p+1$ knots. A total of $n = m - p - 1$ NURBS basis functions (denoted as R_A, with $A = 1, \ \ldots, n$) can be obtained by means of the Cox-de Boor recursion formula (see Piegl and Tiller [24]). Each R_A associates with a control point, analogous to a node in the FEM mesh, allowing geometrical or physical quantities defined in the parametric space $\{\xi \mid \xi \in [\xi_1, \xi_m]\}$ to be interpolated through the corresponding discrete values at the control points. If $\boldsymbol{\Xi}$ contains no repeated interior knots (excluding the first and last $p+1$ knots), the number of non-zero knot spans is $n-p$, which also represents the element number in the NURBS mesh. Each repetition of an interior knot reduces the element number by one.

Since multivariate NURBS basis functions are formed by tensor products of univariate ones, two knot vectors

$$\boldsymbol{\Xi}_f^j = \{\xi_{f1}^j, \xi_{f2}^j, \ \ldots, \xi_{fn_f^j+p_f^j+1}^j\}, \quad j = 1, 2, \tag{25}$$

are required to construct the fluid domain Ω_f for the Reynolds equation. The NURBS basis functions on Ω_f are represented as $R_{fA}(\boldsymbol{\xi}_f)$, with $A = 1, \ \ldots, n_f^1 n_f^2$. Similarly, three knot vectors

$$\boldsymbol{\Xi}_s^{ij} = \{\xi_{s1}^{ij}, \xi_{s2}^{ij}, \ \ldots, \xi_{sn_s^{ij}+p_s^{ij}+1}^{ij}\}, \quad j = 1, 2, 3, \tag{26}$$

are needed to build the solid domain Ω_{st}^i. The corresponding NURBS basis functions are signified as $R_{sA}^i(\boldsymbol{\xi}_s^i)$, with $A = 1, \ \ldots, n_s^{i1} n_s^{i2} n_s^{i3}$.

The parameterization for the unknowns in the EHL model ($\boldsymbol{x}_s^i$, p, and r) and their variations can thus be expressed as

$$\boldsymbol{x}_s^i\big|_{\xi_s^i} = \sum_{A=1}^{n_s^i} \boldsymbol{x}_{sA}^i R_{sA}^i(\xi_s^i), \qquad (\delta \boldsymbol{x}_s^i)\big|_{\xi_s^i} = \sum_{A=1}^{n_s^i} \delta \boldsymbol{x}_{sA}^i R_{sA}^i(\xi_s^i), \tag{27}$$

$$p|_{\xi_f} = \sum_{A=1}^{n_f} p_A R_{fA}(\boldsymbol{\xi}_f), \qquad \delta p|_{\xi_f} = \sum_{A=1}^{n_f} \delta p_A R_{fA}(\boldsymbol{\xi}_f), \tag{28}$$

$$r|_{\xi_f} = \sum_{A=1}^{n_f} r_A R_{fA}(\boldsymbol{\xi}_f), \qquad \delta r|_{\xi_f} = \sum_{A=1}^{n_f} \delta r_A R_{fA}(\boldsymbol{\xi}_f), \tag{29}$$

where $n_f = n_f^1 n_f^2$ and $n_s^i = n_s^{i1} n_s^{i2} n_s^{i3}$ indicate the number of control points for the fluid and solid meshes, respectively. Additionally, $\boldsymbol{x}_{sA}^i$, p_A, and r_A refer to the discretized values computed at the corresponding control points.

3.2 Variations of the interaction variables in discretized form

To discretize the virtual work $\delta \Pi_{s,c}^i$ in Eq. (23), the variation of the key interaction quantities must first be discretized. Substituting the discretized form of $\delta \boldsymbol{x}_s^i$ in Eq. (27) into Eq. (A.4) results in

$$\delta\bar{x}_{sn}^{i} = \left(\delta\boldsymbol{x}_{s}^{i}\right)\big|_{\bar{\boldsymbol{\xi}}_{s}^{i}} \cdot \bar{\boldsymbol{n}}^{i} = \left[\sum_{A=1}^{n_s^i} \delta\boldsymbol{x}_{sA}^{i} R_{sA}^{i}\left(\bar{\boldsymbol{\xi}}_{s}^{i}\right)\right] \cdot \bar{\boldsymbol{n}}^{i} = \sum_{A=1}^{n_s^i} \delta\boldsymbol{x}_{sA}^{i} \cdot \left[R_{sA}^{i}\left(\bar{\boldsymbol{\xi}}_{s}^{i}\right)\bar{\boldsymbol{n}}^{i}\right]. \tag{30}$$

It should be noted that the convective coordinate $\bar{\boldsymbol{\xi}}_{sI}^{i} = \left(\bar{\xi}_{sI}^{i1}, \bar{\xi}_{sI}^{i2}\right)$ in Eq. (A.2) is attached to the interaction surface Γ_{It}^{i}, making it two-dimensional. However, when using the knots from Eq. (26) as the convective coordinate to describe the projection point, it becomes three-dimensional. In this case, $\bar{\boldsymbol{\xi}}_{s}^{i} = \left(\bar{\xi}_{sI}^{i1}, \bar{\xi}_{sI}^{i2}, \bar{\xi}_{sI}^{i3}\right)$, where $\bar{\xi}_{sI}^{i3}$ represents the knot for Γ_{It}^{i} in the orthogonal dimension.

Similar discretization procedures can be applied to other variations in Eq. (23). After introducing the auxiliary vectors in Appendix A, $\delta\bar{x}_{sn}^{i}$, $\delta\bar{x}_{ss1}^{i}$, and $\delta\bar{x}_{ss2}^{i}$ in Eqs. (A.4)-(A.6) can be formulated in matrix form as

$$\delta\bar{x}_{sn}^{i} = \delta\boldsymbol{x}^{iT}\boldsymbol{N}^{i}, \tag{31}$$

$$\delta\bar{x}_{ss1}^{i} = \delta\boldsymbol{x}^{iT}\left[\boldsymbol{C}_{u}^{i} + \left(\bar{\boldsymbol{\tau}}_{\alpha}^{i} \cdot \boldsymbol{U}_{sd}\right)\boldsymbol{D}_{\alpha}^{i}\right], \tag{32}$$

$$\delta\bar{x}_{ss2}^{i} = \delta\boldsymbol{x}^{iT}\left[\boldsymbol{C}_{p}^{i} + \left(\bar{\boldsymbol{\tau}}_{\alpha}^{i} \cdot \nabla p\right)\boldsymbol{D}_{\alpha}^{i}\right]. \tag{33}$$

3.3 Mortar-based formulation for the interaction virtual work

Generally, the fluid domain Ω_f needs to be discretized with a finer mesh than Γ_{It}^{i} from the solid part to better capture the complex cavitation phenomena. The mortar method is employed here to achieve such non-matching meshes at the interaction interface. The solid bodies are assigned as the mortar sides, while Ω_f is chosen as the non-mortar side.

As suggested in Tur et al. [41] and de Lorenzis et al. [20], the integration in Eq. (23) is conducted on the non-mortar side (Ω_f) without additional segmentation of the overlapping meshes between Ω_f and Γ_{It}^{i} to avoid the associated computational costs. Although this approach may introduce errors for irregularly shaped overlapping meshes, these errors can be minimized by increasing the number of integration points within the NURBS elements on Ω_f. The transformation of the integration domain in Eq. (23) can be accomplished using a surface element factor $\bar{J}_{sf}^{i}$:

$$\delta\Pi_{s,c}^{i}=\int_{\Omega_f}\delta\bar{x}_{sn}^{i}p\bar{j}_{sf}^{i}\,\mathrm{d}\Omega+(-1)^{i}\eta\int_{\Omega_f}\delta\bar{x}_{ss1}^{i}\frac{1}{h}\bar{j}_{sf}^{i}\,\mathrm{d}\Omega+\frac{1}{2}\int_{\Omega_f}\delta\bar{x}_{ss2}^{i}h\bar{j}_{sf}^{i}\,\mathrm{d}\Omega, \tag{34}$$

with

$$\bar{j}_{sf}^{i}=\left\|\frac{\partial\bar{\boldsymbol{x}}_{s}^{i}}{\partial x}\times\frac{\partial\bar{\boldsymbol{x}}_{s}^{i}}{\partial y}\right\|=\sqrt{1+\left\|\nabla\bar{z}_{s}^{i}\right\|^{2}}. \tag{35}$$

Following the principles of the mortar method [20, 26], the discretized interaction virtual work is formulated as

$$\delta\Pi_{s,c}^{i}=\sum_{A=1}^{n_f}\left[\delta\bar{x}_{snA}^{i}p_A+(-1)^{i}\eta\frac{\delta\bar{x}_{ss1A}^{i}}{h_A}+\frac{1}{2}\delta\bar{x}_{ss2A}^{i}h_A\right]\bar{j}_{sfA}^{i}A_A\,, \tag{36}$$

where the summation runs over all control points in the NURBS discretization of the fluid domain. All these averaged quantities associated with the control points (with subscript A denoting the control point index), together with their discretizations, are provided in Appendix A. Consequently, the discretized virtual work $\delta\Pi_{s,c}^{i}$ in Eq. (36) is thus reformulated as

$$\delta\Pi_{s,c}^{i}=\delta\boldsymbol{x}^{iT}\bar{\boldsymbol{R}}_{x}^{ic}, \tag{37}$$

with $\bar{\boldsymbol{R}}_{x}^{ic}$ computed through

$$\bar{\boldsymbol{R}}_{x}^{ic}=\sum_{A=1}^{n_f}\left[p_A\bar{j}_{sfA}^{i}\boldsymbol{L}_{nA}^{i}+(-1)^{i}\eta\frac{\bar{j}_{sfA}^{i}}{h_A}\boldsymbol{L}_{uA}^{i}+\frac{1}{2}h_A\bar{j}_{sfA}^{i}\boldsymbol{L}_{pA}^{i}\right]. \tag{38}$$

The residual vector $\bar{\boldsymbol{R}}_{x}^{ic}$, contributed by the interaction between the lubricant and solids, can be incorporated into the global residual vector, allowing the unknowns to be solved through the Newton-Raphson method. The corresponding Jacobian matrices are derived by linearizing Eq. (36), with the results documented in Appendix B to keep the main text concise.

4 Benchmark tests

In this section, the accuracy and quality of the proposed model are demonstrated via benchmark tests involving EHL contact between an elastic cylinder (radius $R=10$ mm) and a rigid plane. The

cylinder is first assumed to be composed of a hard material with a high elastic modulus ($E_{cyl} = 105$ GPa), leading to negligible deformation in the contact region relative to its length in the y-direction. This three-dimensional case can thus be simplified to a two-dimensional plane strain configuration (corresponding to the hard EHL line contact), as illustrated in Fig. 4.

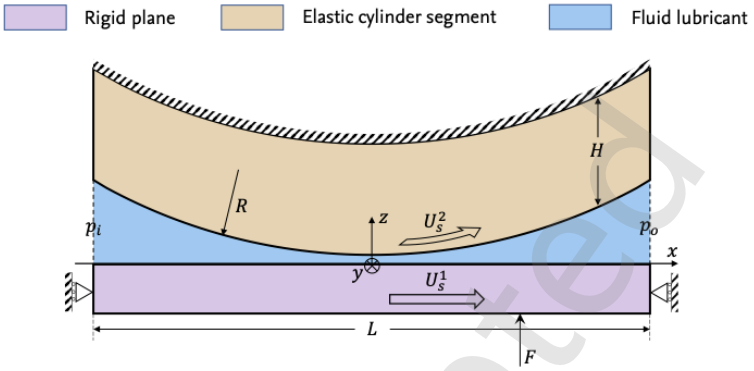

Fig. 4 EHL line contact between an elastic cylinder and a rigid plane.

In this configuration, the cylinder rotates at velocity U_s^2 while the plane moves at velocity U_s^1, with both velocities equal ($U_s^1 = U_s^2$). Given the negligible shear stress in such a pure rolling condition, only normal forces acting on the solid surface are considered. Additionally, the full cylinder is simplified to a segment ($L = 10$ mm, $H = 2$ mm) due to the small pressurized area. Consequently, the vertical velocity component of the cylinder can be disregarded owing to the small curvature of the segment. Furthermore, deformations of material points far from the center are minimal, which is equivalent to a fixed upper boundary. The external vertical load F is then applied to the bottom of the rigid plane, which is unconstrained in the z-direction.

The lubricant is assumed to be incompressible in this analysis. However, due to the high pressure in hard EHL contacts, the lubricant's piezo-viscous properties are taken into account. The viscosity-pressure relationship is governed by the widely applied Barus equation $\eta = \eta_0 e^{\alpha p}$, where α is a constant coefficient. The inlet and outlet pressures are prescribed as $p_i = p_o = 5000$ Pa to achieve the fully flooded condition. Detailed descriptions of all material parameters and boundary conditions relevant to this study are provided in Table 1.

Table 1 Material properties and boundary conditions for the hard EHL line contact.

Parameter	Value
Cylinder elastic modulus	$E_{cyl} = 105$ GPa
Cylinder Poisson's ratio	$\nu_{cyl} = 0.3$
Lubricant base viscosity	$\eta_0 = 0.04$ Pa · s
Pressure-viscosity coefficient	$\alpha = 10^{-8}$ m^2/N
Boundary pressure	$p_i = p_o = 5000$ Pa
Boundary void fraction	$r_i = r_o = 0$
Cylinder velocity	$U_s^2 = 0.5$ m/s
Rigid plane velocity	$U_s^1 = 0.5$ m/s
Vertical line load	$F = 230$ kN/m

For comparison, the commercial software ANSYS is used to generate a reference solution. The lubricant flow and the transition to cavitation bubbles are analyzed using the FVM-based CFD solver, ANSYS *Fluent*, while the cylinder's elastic deformations are calculated with the FEM-based solver, ANSYS *Mechanical*. These two solvers are coupled using an iterative implicit scheme.

The setup for the ANSYS FSI model has been comprehensively described by Singh et al. [30], and will not be repeated here. Nevertheless, a few details are worth mentioning. Importantly, the coupling scheme in ANSYS supports only three-dimensional calculations, meaning the two-dimensional geometries from Fig. 4 must be converted into three-dimensional structures by adding a thin layer along the y-direction. Symmetry boundary conditions are applied to the front and back surfaces of this layer to maintain the plane strain condition.

The meshing process also deserves special attention. The cylinder is meshed using the 20-node *SOLID186* element, while the fluid domain is meshed with the 8-node *HEX8* element (see Fig. 5a). These elements will be referred to as P2 and P1 elements, respectively, corresponding to their quadratic and linear polynomial basis functions. A key requirement for ANSYS FSI models is that the mesh on the interaction surface must be conformal, meaning the fluid and structure components' elements must be precisely aligned at the interaction interface.

Moreover, mesh refinement in the potential contact region is crucial for accurately capturing deformations and pressure distributions in the hard EHL contact regime. This region is approximated using the well-known Hertzian theory, which offers an analytical solution for pure solid contacts undergoing small deformations (detailed in Popov [25]). The half-width a of the Hertzian contact region is derived through

$$a = \sqrt{\frac{4FR}{\pi E^*}}, \qquad E^* = \frac{E_{cyl}}{1 - \nu_{cyl}^2}. \tag{39}$$

Based on the mesh sensitivity analysis from Singh et al. [30], seeding 500 elements along the interaction surface is sufficient to achieve convergent solutions. Of these, 200 elements are uniformly distributed within the potential contact region (in this case, $a = 0.16$ mm), while the remaining 300 elements are distributed gradient-wise away from the central area, as shown in Fig. 5a. In total, the cylinder segment is meshed with 10000 $P2$ elements (using 72603 nodes), and the fluid domain contains 4000 $P1$ elements (with 9018 nodes).

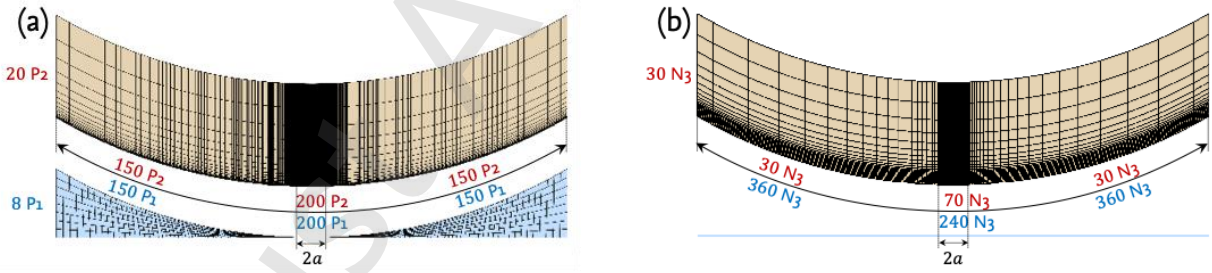

Fig. 5 (a) Mesh used in the ANSYS FSI model (P2: 20-node *SOLID186* elements, P1: 8-node *HEX8* elements). (b) Mesh used in the NURBS-based EHL model

In contrast to the ANSYS FSI model, the EHL model presented in this work reduces the fluid domain to a line by applying the Reynolds equation. The geometries and meshes for both solid and fluid components are generated using NURBS parameterization, eliminating the need for a separate meshing process. NURBS discretization also enables the elevation of polynomial orders to any

desired level without a significant increase in control points (for further details, see the k-refinement method described in Cottrell et al. [7]).

In this example, third-order NURBS (N3) discretizations are applied to both the solid and fluid domains, as shown in Fig. 5b. The meshes are refined in the central area and distributed in gradient patterns outward. Notably, the need for a conformal mesh at the interaction interface is avoided due to the use of mortar-based formulations. The final mesh consists of 2600 N3 elements (with 3059 control points) in the solid domain and 960 N3 elements (with 963 control points) in the fluid domain.

Both models were executed on a single-core processor (*Intel Core i5*, 3.3 GHz) with 16 gigabytes of RAM. The ANSYS model required around 28 hours to converge, whereas the newly developed model finished in approximately 20 minutes. This significant reduction in computational time is mainly attributed to the fewer degrees of freedom in the NURBS-based model. Additionally, its monolithic coupling of the fluid and solid components ensures rapid convergence, achieving the desired external load within 25 load steps. Conversely, the ANSYS model uses sequential fluid and solid solvers, needing up to 9000 load steps to avoid non-convergence at intermediate stages.

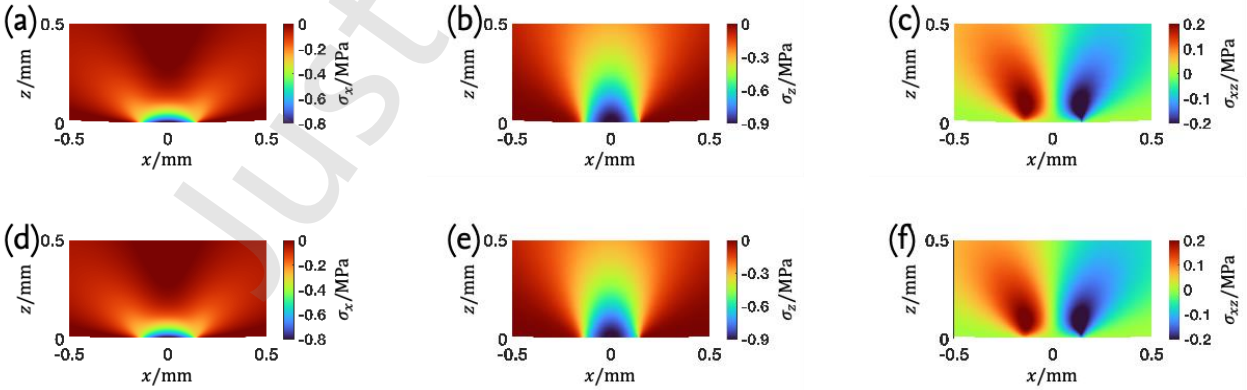

Fig. 6 Cauchy stresses (a) σ_x, (b) σ_z, and (c) σ_{xz} predicted by the ANSYS FSI model; Cauchy stresses (d) σ_x, (e) σ_z, and (f) σ_{xz} predicted by the NURBS-based EHL model.

Figs. 6a-c depict the Cauchy stresses σ_x, σ_z, and σ_{xz} near the pressurized area, respectively, as calculated by the ANSYS FSI model. These stress contours are similar to those observed in Hertzian

contact scenarios, such as the case study presented in de Lorenzis et al. [21] and Tong et al. [37]. This similarity aligns with expectations, as the EHL contact is also a type of contact regime, though mediated through a lubricant layer.

Despite utilizing significantly fewer elements and degrees of freedom, the stresses predicted by the NURBS-based model (shown in Figs. 6d-f) exhibit strong agreement with the reference solutions. The model even captures subtle asymmetries in the σ_{xz} distribution, as seen in Figs. 6c and 6f. This superior performance is largely due to the inherent smoothness and computational efficiency of NURBS discretizations.

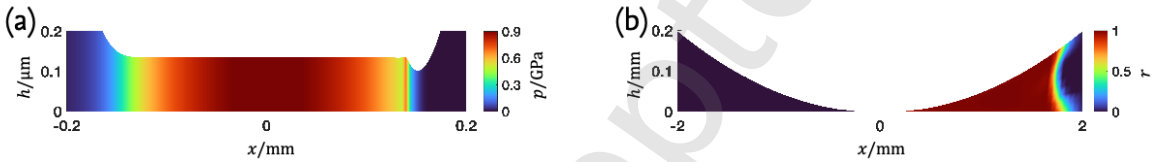

Fig. 7 (a) Pressure and (b) void fraction distributions in the fluid domain computed by the ANSYS FSI model.

Fig. 7 displays the pressure and void fraction distributions obtained from the ANSYS FSI model. The continuous, band-shaped pressure contour in Fig. 7a shows an absence of a pressure gradient along the height direction, confirming the suitability of the Reynolds equation for EHL problems. Notably, the deformed upper surface flattens in the central contact area, reminiscent of Hertzian contact. However, a key distinction is visible at the outlet of the contact region, where film thickness decreases sharply, primarily due to the requirement of maintaining flow continuity.

Table 2 Mesh Parameters for the ANSYS FSI and NURBS-Based EHL Models (CP denotes control point)

Model	**Solid mesh**		**Fluid mesh**	
	Element number	**Node/CP number**	**Element number**	**Node/CP number**
ANSYS FSI	10000 P2	72603	4000 P1	9018
NURBS (Coarse)	1750 N3	2044	720 N3	723
NURBS (Medium)	3900 N3	4389	960 N3	963
NURBS (Fine)	5600 N3	6194	1200 N3	1203

The fluid solutions obtained from the ANSYS model cannot be directly compared to those from the EHL model based on the Reynolds equation. Thus, the pressure and void fraction distributions in Fig. 7 must first be averaged along the height direction. Aside from the NURBS mesh depicted in Fig. 5b, the EHL model also employs a coarser and a finer NURBS mesh. The number of elements and nodes (or control points in NURBS meshes) for each mesh configuration are detailed in Table 2.

Fig. 8a presents the pressure distributions obtained by the EHL model with NURBS meshes of three different resolutions against the reference solution from the ANSYS FSI model. A pressure distribution based on Hertzian contact theory [25] is also provided. The radius of the EHL contact area, where fluid pressure builds and deforms the solid, is approximately $a_{EHL} = 0.16$ mm, which is nearly identical to the Hertzian contact radius. In the central region, where the peak pressure is located, the ANSYS and NURBS solutions align closely with the Hertzian analytical solution, demonstrating that the EHL contact shares similarities with direct solid contacts.

The solutions from the newly developed model show good alignment with the ANSYS results across different mesh resolutions. The medium and fine NURBS meshes accurately capture the pressure spike near the outlet, while the coarse mesh produces minor oscillations near the spike, likely due to the steep pressure gradient. Despite this, it is notable that the coarse mesh computations are completed in just 10 minutes.

Fig. 8b shows the void fraction distributions determined by the ANSYS and EHL models. The NURBS-based model accurately captures the cavitation region, with even the coarse mesh yielding high-quality results. Nevertheless, slight discrepancies between the EHL and ANSYS solutions are visible. These differences stem from the cavitation model used in the ANSYS CFD solver, which is based on bubble dynamics and phase transitions.

Fig. 8c compares the deformed gap height distributions near the contact region as calculated by both models. The profiles obtained from the NURBS-based model visually follow the ANSYS reference curve very closely, indicating that the model captures the correct deformation trend.

Notably, despite the unphysical pressure oscillations induced by the coarse NURBS mesh, the resulting deformed gap height remains consistent with the finer-mesh and ANSYS results.

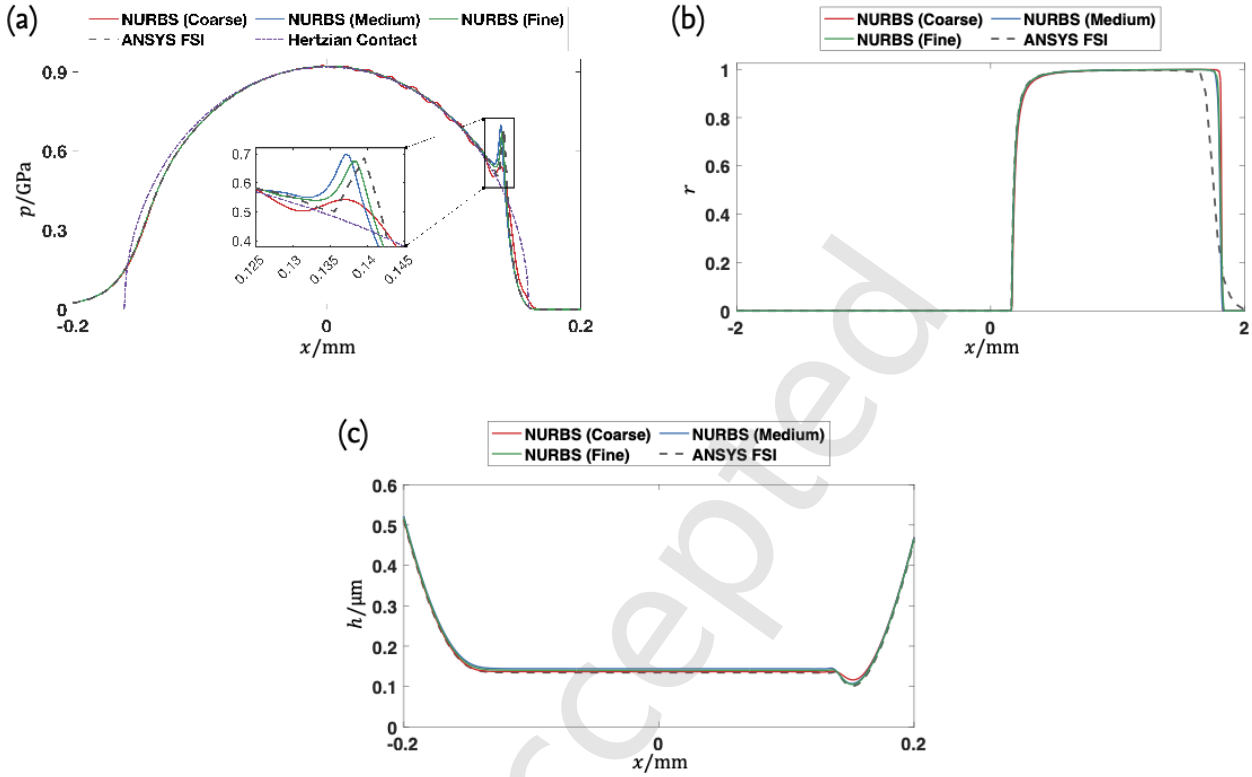

Fig. 8 Comparison of the (a) averaged pressure, (b) void fraction, and (c) deformed gap height between the ANSYS FSI model and the NURBS-based EHL model.

To further quantify the model accuracy and assess its mesh sensitivity, Table 3 presents the relative errors of representative quantities evaluated against the ANSYS reference solution. The examined quantities include the maximum pressure as well as the central and minimum gap height, which are characteristic indicators of EHL performance. The overall decrease in error with mesh refinement demonstrates the convergence and reliability of the new model. The results also confirm that the coarse mesh already provides accurate predictions for maximum pressure and central gap height. However, because the minimum gap height is extremely small, even a minor deviation in absolute value results in a relatively large percentage error for the coarse mesh.

Table 3 Mesh-sensitivity assessment of the NURBS-based EHL model with relative errors evaluated against the ANSYS reference solution.

Mesh resolution	Evaluated error		
	Max. pressure	Central gap height	Min. gap height
Coarse	0.08%	1.59%	14.88%
Medium	0.02%	6.95%	5.77%
Fine	0.01%	4.17%	3.80%

For completeness, the FVM-based EHL-FBNS model [12] was tested on the same hard EHL line-contact benchmark. Using a uniform grid of 2048 cells, the EHL-FBNS solver did not reach convergence even after extensive iterations. This difficulty arises because the present benchmark contains a highly localized EHL contact region ($a_{EHL} = 0.16$ mm) embedded within a fluid domain of approximately 10 mm length. Resolving the steep pressure spike and the cavitation zone in such cases requires pronounced local mesh refinement, which the uniform-grid EHL-FBNS implementation does not provide. In the absence of refinement, the method would require prohibitively fine global discretization to adequately capture the local gradients.

After demonstrating the superiority of the proposed model in addressing hard EHL contact problems, this section will illustrate its capability in handling soft EHL contacts, where the nonlinear behavior of the solid material is taken into account. For this purpose, the setup shown in Fig. 4 is retained, but the cylinder material is replaced by a soft rubber characterized by an elastic modulus of $E_{cyl} = 2.4$ MPa and a Poisson's ratio of $\nu_{cyl} = 0.49$. In ANSYS, the default Neo-Hookean material model is typically employed to describe the hyperelastic response of rubber, with the constitutive relation expressed as

$$\boldsymbol{S} = \mu(\boldsymbol{I} - \boldsymbol{C}^{-1}) + \kappa J(J-1)\boldsymbol{C}^{-1}. \quad (40)$$

In this formulation, $\boldsymbol{S}$ and $\boldsymbol{C}$ denote the second Piola–Kirchhoff stress tensor and the right Cauchy–Green tensor, respectively, while J represents the determinant of the deformation gradient. The Lamé parameter μ and the bulk modulus κ are determined from

$$\mu = \frac{E_{cyl}}{2(1+\nu_{cyl})}, \quad \kappa = \frac{E_{cyl}}{3(1-2\nu_{cyl})}. \tag{41}$$

To clearly demonstrate the highly nonlinear characteristics of this constitutive law, Fig. 9 compares the uniaxial stress–strain curve obtained from Eq. (40) with that predicted by a linear elastic law using identical values of E_{cyl} and ν_{cyl}. The results show that the linearly elastic law substantially overestimates the stress level at large strains (e.g., engineering strains exceeding 10% in Fig. 9). For soft EHL contact problems, which involve more complex deformation states than uniaxial loading, employing a hyperelastic description is therefore essential.

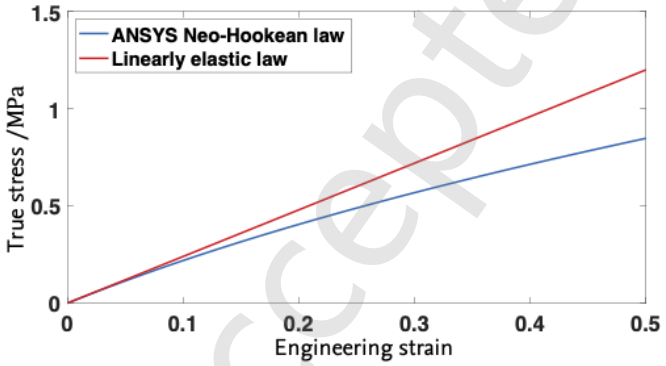

Fig. 9 Comparison of the uniaxial stress–strain response predicted by the ANSYS Neo-Hookean law and the linearly elastic law for identical material parameters ($E_{cyl} = 2.4$ MPa, $\nu_{cyl} = 0.49$).

The vertical line load is adjusted to 800 N/m, which, according to Eq. (39), results in a half-width of the contact region approximately ten times larger than that of the hard EHL contact problem described above. Consequently, the centrally refined region in the ANSYS FSI model (see Fig. 5) must be enlarged, while the type and the total number of elements remain unchanged. It should also be noted that the "large deflection" option in ANSYS Mechanical must be activated to capture the nonlinear deformation response. This setting, however, further slows down convergence, and the ANSYS FSI model ultimately required about 42 hours of computation. By contrast, the proposed model employed the coarse NURBS mesh listed in Table 2 and completed the calculation in about 120 iterations and 12 minutes of runtime.

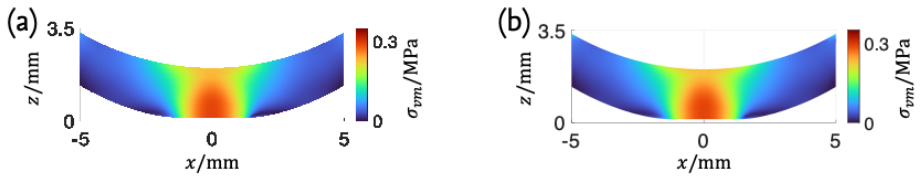

Fig. 10 Von Mieses stress σ_{vm} considering cylinder hyperelasticity, predicted by (a) the ANSYS FSI model and (b) the NURBS-based EHL model.

Fig. 10 compares the Von Mises stress distributions within the hyperelastic cylinder, as obtained from the ANSYS FSI model and the newly proposed model. Owing to the much lower stiffness of the cylinder, the deformation region becomes significantly larger than in the hard EHL contact case, while the stress level is markedly smaller. It can also be observed that, despite the proposed model requiring only about 0.5% of the computational time of the ANSYS model, both approaches yield quantitatively consistent stress patterns, further highlighting the superiority of the NURBS-based model.

Fig. 11 presents a more detailed comparison of the results obtained from the two models. Notably, in order to illustrate the effects of nonlinear deformation, results computed using the NURBS-based model with linear elasticity (LE) are also included in Fig. 11 (red lines). Compared with the NURBS-based model with hyperelasticity (HE), the LE formulation represents a simplified variant: the configuration changes in Eq. (16) are neglected (using the Cauchy stress instead of the Piola-Kirchhoff stress), and the solid behavior is described by a linearly elastic law (see Fig. 9).

In fact, the FVM-based EHL-FBNS model [12] was also tested for this soft EHL configuration. The solver required about 21450 iterations and roughly 35 minutes to converge, which does not provide a computational advantage over the proposed NURBS-based formulation. Moreover, because the EHL–FBNS approach relies on a half-space approximation to evaluate solid deformation, it does not explicitly capture the actual cylinder curvature. As a consequence, the predicted pressure and gap-height fields showed noticeable deviations from both the ANSYS reference solution and the NURBS-based results. For these reasons, the FBNS results are not included here, and the NURBS-

based model with linear elasticity (LE), which converges within roughly 100 iterations and about 8 minutes, is used instead as a consistent reference for assessing the influence of nonlinear deformation.

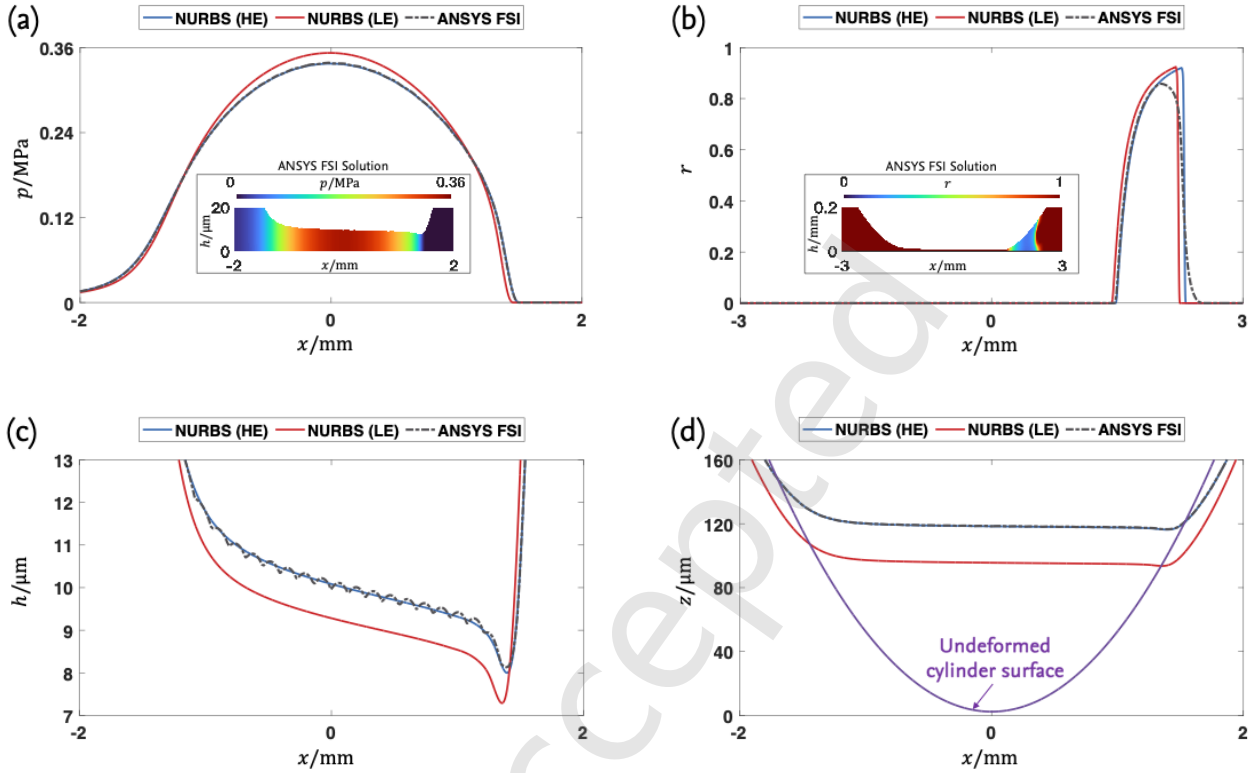

Fig. 11 Comparison of the (a) averaged pressure, (b) void fraction, (c) deformed gap height, and (d) deformed cylinder surface among the ANSYS FSI model, the NURBS-based model with hyperelasticity (HE), and the NURBS-based model with linear elasticity (LE).

As can be seen from Fig. 11, the results predicted by the HE model are in excellent agreement with those obtained from ANSYS. Using only the coarse mesh listed in Table 2, the proposed model accurately captures the location and extent of the cavitation region. The deformed gap height computed by ANSYS shows minor numerical oscillations in the central region, but this does not affect its overall consistency with the NURBS results. A small discrepancy can be observed in the peak value of the cavitation volume fraction, which is slightly higher in the ANSYS solution. This difference arises because ANSYS models cavitation based on bubble dynamics, where the void fraction is treated as a function of the local film thickness.

In contrast, the results obtained using the infinitesimal strain theory deviate significantly. As shown in Fig. 11a, the model with linear elasticity predicts a higher pressure-peak compared to the nonlinear case, while Fig. 11d clearly indicates a smaller deformation of the cylinder surface. This behavior is consistent with Fig. 9, where the linearly elastic law markedly underestimates the material's deformation capacity compared to the hyperelastic formulation.

Table 4 Relative errors of key quantities in the soft EHL line contact, evaluated against the ANSYS reference solution for the NURBS-based model using hyperelastic (HE) and linear-elastic (LE) material laws.

Material model	Evaluated error			
	Max. pressure	Central gap height	Min. gap height	Central deformation
LE	4.25%	6.81%	10.36%	19.25%
HE	0.22%	1.25%	1.61%	0.02%

To explicitly assess the numerical accuracy of the two material formulations, Table 4 lists the relative errors of the maximum pressure, the central and minimum gap heights, and the central deformation with respect to the ANSYS reference solution. The hyperelastic model reproduces the ANSYS results with excellent accuracy, yielding relative errors below 2% for both pressure and film thickness. In contrast, the linear-elastic model exhibits markedly larger deviations, particularly in the predicted deformation, where the relative error exceeds 19%. These discrepancies are expected to become more pronounced with increasing external load. Therefore, employing a realistic constitutive law in combination with a nonlinear deformation framework is essential for accurately modeling soft EHL contact problems.

5 Soft EHL point contact

In this section, the newly developed model is applied to investigate the EHL contact between an hyperelastic hemisphere and a rigid plane (see Fig. 12). A fluid lubricant is introduced to separate the contact surfaces and balance the external vertical load F. The hemisphere, with a radius of $R = 10$ mm, is fixed at its upper surface ($U_s^2 = 0$), while the rigid plane moves at a constant velocity U_s^1. Therefore, the entraining velocity is evaluated as $\bar{U}_s = U_s^1/2$.

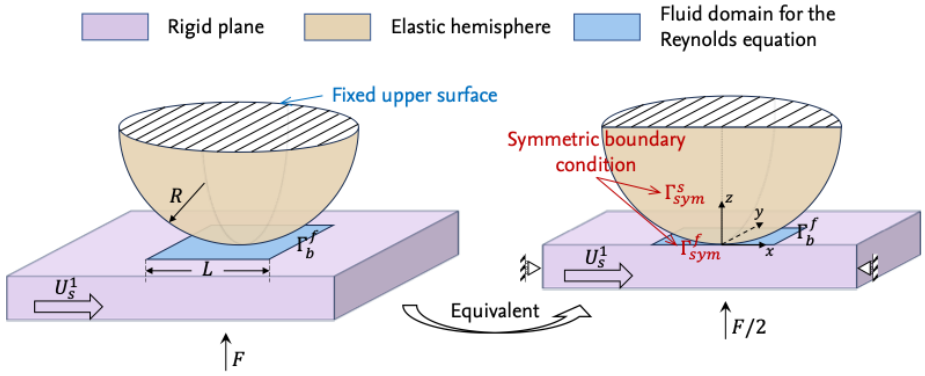

Fig. 12 Soft EHL point contact between an elastic hemisphere and a rigid plane.

The fluid domain corresponding to the Reynolds equation is defined as a square with a side length of $L = 10$ mm, ensuring that its boundary Γ_b^f is sufficiently far from the central contact area. The boundary conditions for the pressure p_b and void fraction r_b at Γ_b^f are set as

$$p_b = 0 \text{ Pa}, \quad r_b = 0, \quad \forall x_f \in \Gamma_b^f, \tag{42}$$

to establish a fully flooded condition.

Additionally, to efficiently reduce computational cost, symmetry boundary conditions are imposed on the symmetry plane Γ_{sym}^s of the solid hemisphere and the symmetry axis Γ_{sym}^f of the fluid domain (refer to the equivalent problem depicted in Fig. 12):

- For all material points on Γ_{sym}^s, the displacement in the y-direction is constrained to zero,

$$u_{sy}^2 = 0, \quad \forall \boldsymbol{x}_s^2 \in \Gamma_{sym}^s. \tag{43}$$

- For all spatial points on Γ_{sym}^f, the flow velocity in the y-direction is set to zero, indicating a zero pressure-gradient,

$$\frac{\partial p}{\partial y} = 0, \quad \forall \boldsymbol{x}_f \in \Gamma_{sym}^f. \tag{44}$$

This study employs a different form of the constitutive law from that in Eq. (40) introduced in the previous section. It also belongs to the Neo-Hookean family and is used to describe the nonlinear elastic response of the hemisphere:

$$\boldsymbol{S} = \mu(\boldsymbol{I} - \boldsymbol{C}^{-1}) + \lambda(ln\,J)\boldsymbol{C}^{-1}. \quad (45)$$

The Lamé parameters λ and μ are derived from Young's modulus E_s and Poisson's ratio ν_s:

$$\lambda = \frac{E_s \nu_s}{(1+\nu_s)(1-2\nu_s)}, \quad \mu = \frac{E_s}{2(1+\nu_s)}. \quad (46)$$

For this soft EHL scenario, a rheological law for pressure-dependent viscosity is not required, since the fluid pressure remains relatively low (as can be seen from Fig. 11a). Accordingly, the lubricant is treated as isoviscous, with a viscosity of $\eta = 0.78$ Pa · s. The complete set of default parameters for this case is provided in Table 5.

Table 5 Material properties and default boundary conditions for the EHL point contact

Parameter	Value
Hemisphere radius	$R = 10$ mm
Hemisphere elastic modulus	$E_s = 2.4$ MPa
Hemisphere poisson's ratio	$\nu_s = 0.49$
Lubricant viscosity	$\eta = 0.78$ Pa · s
Boundary pressure	$p_b = 0$ Pa
Boundary void fraction	$r_b = 0$
Entraining velocity	$\bar{U}_s = 0.1$ m/s
Vertical load	$F = 10$ N

The quarter sphere and the rectangular fluid domain depicted in Fig. 12 can each be represented using a single NURBS element. To ensure a uniform NURBS structure, a non-zero inner radius is introduced for the quarter sphere. This radius is sufficiently small (1 mm) to avoid influencing the results, as shown in Fig. 13. Since the construction process is not the primary focus of this study, it is not detailed here. Readers seeking additional information may refer to Piegl and Tiller [24].

The NURBS meshes for both the solid and fluid domains are then elevated to third-order NURBS (N3) parameterizations across all dimensions (see Fig. 13). Local refinement is applied to the solid mesh in the central pressurized area to accurately capture large deformations. Ultimately, the quarter sphere consists of $40 \times 20 \times 10 = 8000$ elements (corresponding to $43 \times 23 \times 13 = 12857$ control points), while the fluid domain is composed of $80 \times 40 = 3200$ N3 elements (corresponding

to $83 \times 43 = 3569$ control points). Additional mesh-refinement tests did not lead to noticeable changes in the predicted pressure, film-thickness or deformation fields, indicating that the chosen discretization is numerically well resolved for this 3D configuration.

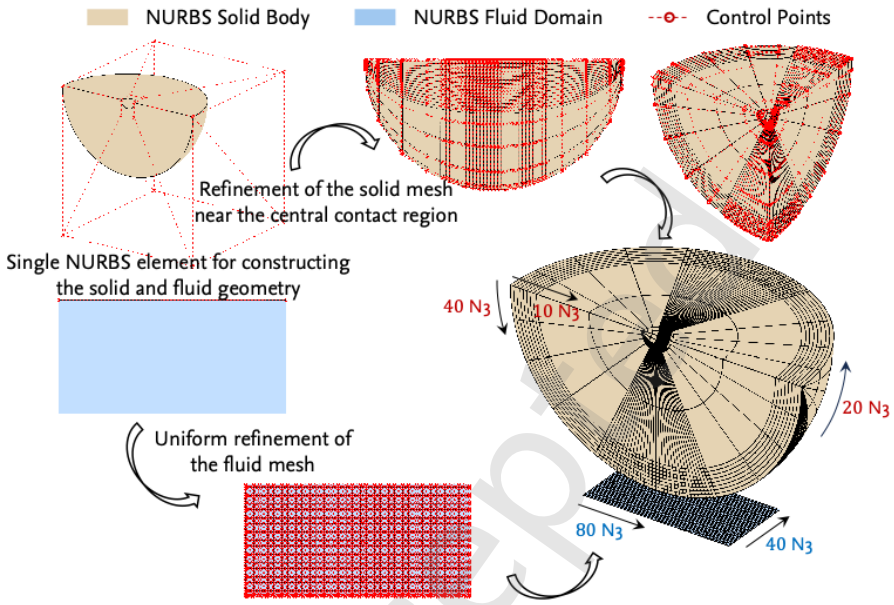

Fig. 13 NURBS mesh utilized for the soft EHL point contact problem.

Fig. 14 illustrates the stress distributions within the deformed hemisphere under the fully flooded condition ($F = 10$ N, $\bar{U}_s = 0.1$ m/s), as predicted by the NURBS-based EHL model. It is observed that all stress components exhibit nearly complete symmetry about the yz-plane, including the shear stress σ_{zx}. This behavior deviates from that typically observed in hard EHL contacts, where subtle asymmetries are present (see Fig. 6f). This deviation can be attributed to the significantly softer material of the hemisphere, which contrasts with hard EHL cases and prevents the formation of a pressure spike, as shown in Fig. 8a. Consequently, soft EHL contact more closely resembles Hertzian contact patterns (e.g. in de Lorenzis et al. [21]) compared to hard EHL contact.

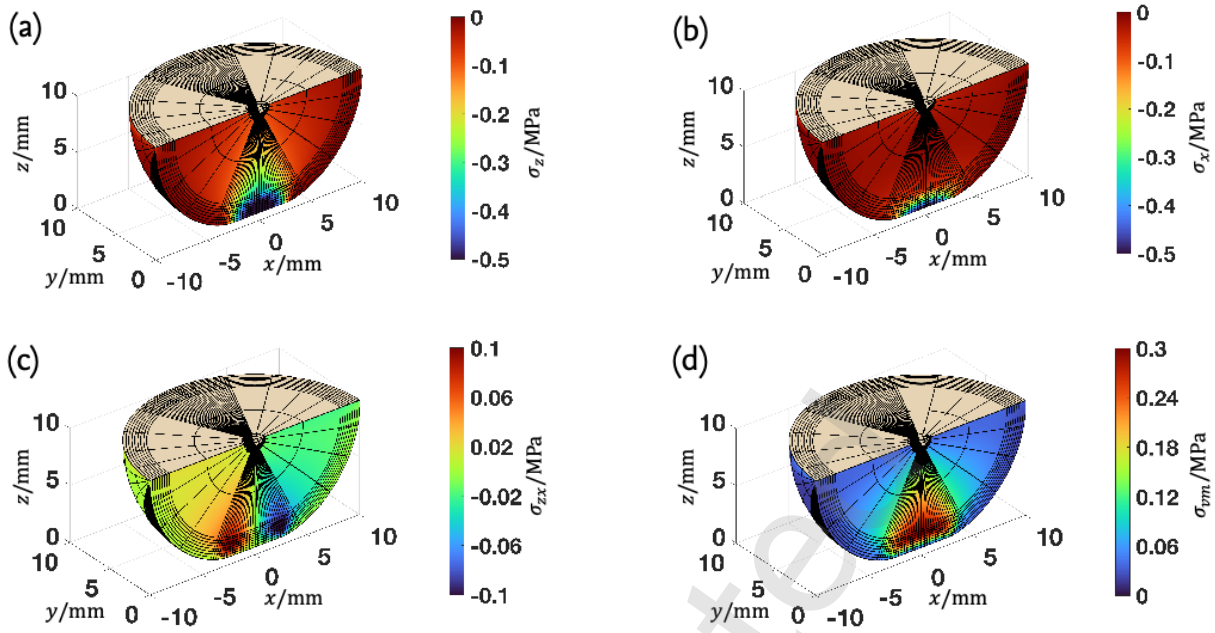

Fig. 14 Stresses within the deformed hemisphere under the fully flooded condition with an external load $F = 10$ N and entraining velocity $\overline{U}_s = 0.1$ m/s, obtained from the NURBS-based EHL model: (a) normal stress σ_z, (b) normal stress σ_x, (c) shear stress σ_{zx}, and (d) Von Mises stress σ_{vm}.

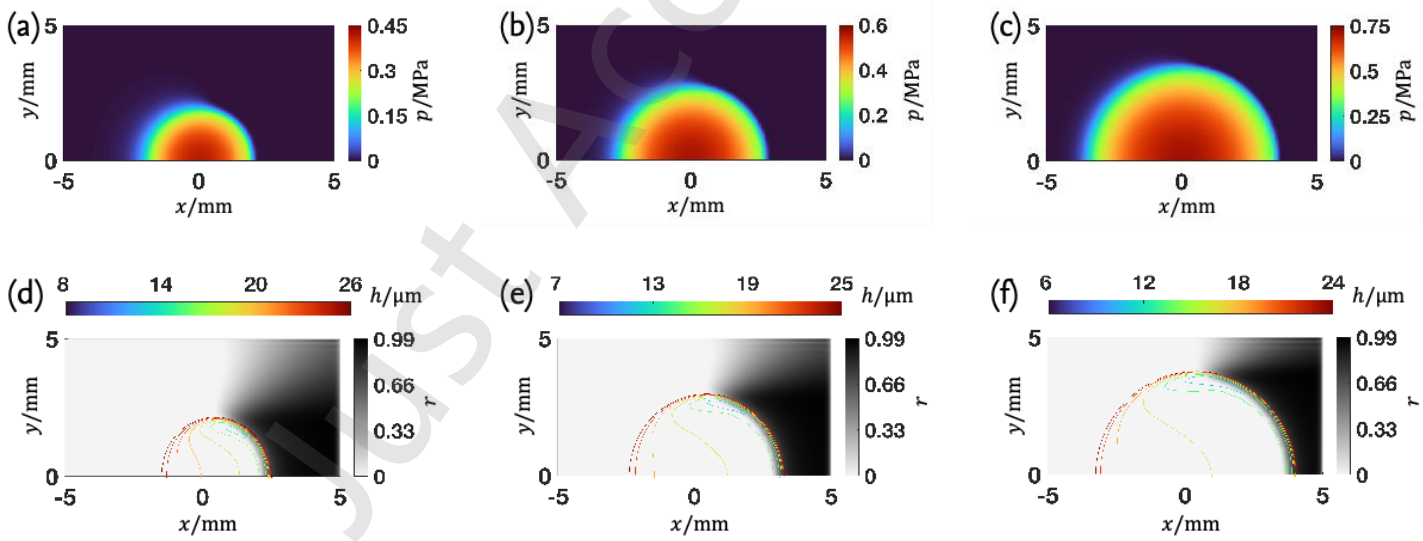

Fig. 15 Pressure p (a-c), void fraction r (grayscale, d-f), and deformed gap height h (color contours, d-f) under the fully flooded condition, obtained from the NURBS-based EHL model. Subplots correspond to different external loads: (a, d) $F = 4$ N, (b, e) $F = 10$ N, and (c, f) $F = 20$ N, with entraining velocity corresponding to different external loads (entraining velocity $\overline{U}_s = 0.1$ m/s).

Fig. 15 shows the distributions of pressure, void fraction, and deformed gap height within the fluid domain, with the entraining velocity maintained at $\overline{U}_s = 0.1$ m/s. In addition to the external load of

$F = 10$ N, which corresponds to the solid stress distributions shown in Fig. 14, this study also investigates two additional loads, $F = 4$ N and $F = 20$ N. Unlike the almost negligible pressurized area in hard EHL contacts (e.g., the pressurized area in Fig. 8a with a radius of 0.16 mm), the EHL contact areas in Figs. 15a-c are relatively large compared to the hemisphere's radius of $R = 10$ mm (e.g. when $F = 10$ N, the radius of the pressurized area is 2.7 mm as shown in Fig. 15b).

Figs. 15d-f clearly demonstrate the presence of a cavitation region on the downstream side. The cavitation region consistently remains adjacent to the central pressurized area. Consequently, as the external load increases, the inner boundary of the cavitation region expands outward along with the pressurized area. Additionally, a larger external load results in a narrower deformed gap height between the hemisphere and the plate.

Moreover, this section examines the effects of varying entraining velocities while maintaining a constant external load. Fig. 16 presents the pressure and gap height profiles for $F = 10$ N, with $\overline{U}_s$ set to 0.1, 0.5, and 2.5 m/s. For comparison, both the NURBS-based model with hyperelasticity (HE) and the NURBS-based model with linear elasticity (LE) are included, with the LE results shown as dashed lines.

Figs. 16a and 16c show that the pressure predicted by the HE and LE models differs significantly. The discrepancy becomes more pronounced as the entraining velocity decreases, with the peak pressure differing by nearly 12% at $\overline{U}_s = 0.1$ m/s. Correspondingly, the deformed gap height obtained from the two models also exhibits noticeable differences. The LE model consistently predicts a smaller gap height, and the deviation from the HE results increases with entraining velocity.

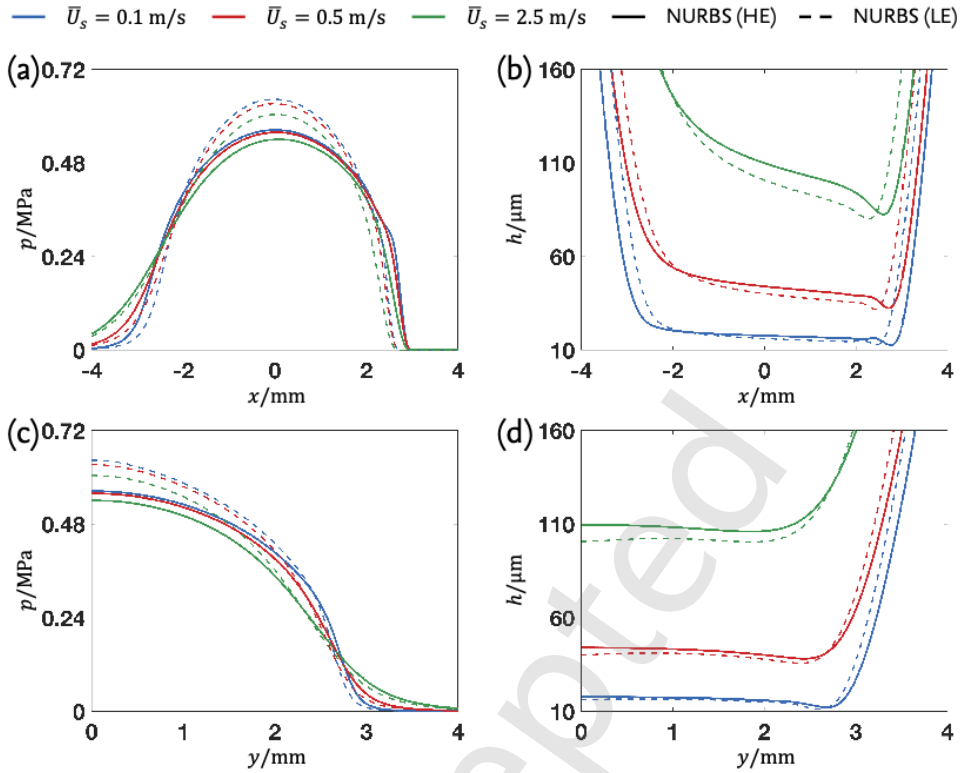

Fig. 16 Pressure and deformed gap height profiles under the fully flooded condition with an external load of $F = 10$ N for various entraining velocities. Subplots show (a) pressure distribution along $y = 0$ mm, (b) gap height profile along $y = 0$ mm, (c) pressure distribution along $x = 0$ mm, and (d) gap height profile along $x = 0$ mm. Solid lines represent the results of the NURBS-based model with hyperelasticity (HE), whereas dashed lines correspond to the NURBS-based model with linear elasticity (LE).

Generally, the deformed central gap height h_{cff}, or central film thickness (these terms are equivalent as the central area is fully filled with lubricant, see Fig. 15d-f), is a key parameter for characterizing EHL point contacts. While the central film thickness for hard EHL contacts can be approximated analytically, an analytical solution for soft EHL contacts is not feasible due to the nonlinear solid deformations. To address this, de Vicente et al. [43] proposed a regression equation for h_{cff} based on extensive numerical simulations under the assumptions of linear elasticity and infinitesimal strain theory:

$$\frac{h_{cff}}{R^*} = 3.3\,\bar{U}^{0.60}\bar{W}^{-0.14}, \tag{47}$$

with $\overline{U} = \overline{U}_s\eta/(E^*R^*)$ and $\overline{W} = F/(E^*R^{*2})$. The reduced radius R^* is equal to R, and the reduced elastic modulus E^* is equal to $2E_s/(1-\nu_s^2)$.

Fig. 17a illustrates the central film thickness h_{cff} for external loads ranging from 0.2 to 20 N, with entraining velocities $\overline{U}_s$ of 0.1, 0.5, and 2.5 m/s. The results of both the NURBS-based hyperelastic (HE) and linear elastic (LE) models are shown, together with the regression equation (77). Since the external load range used by de Vicente et al. [43] was 0.75 to 24 N, their regression equation and the LE model exhibit overall consistent trends within this interval, whereas it is no longer valid for loads below 0.75 N.

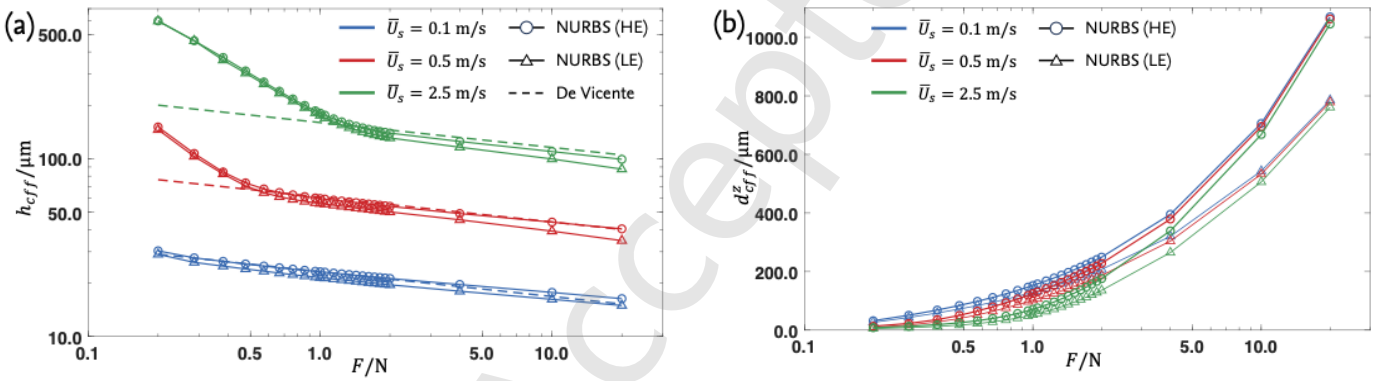

Fig. 17 Results under the fully flooded condition for varying entraining velocities and external loads: (a) central film thickness and (b) central deformation in the z-direction. Circular markers denote the NURBS-based model with hyperelasticity (HE), triangular markers represent the NURBS-based model with linear elasticity (LE), and dashed lines correspond to Eq. (47) from [43].

For loads smaller than 0.75 N, the HE and LE models yield nearly identical values of h_{cff}. This agreement is explained by the minimal deformation of the hemisphere, as illustrated in Fig. 17b, where the central deformation in the z-direction from both NURBS models is shown. Under such conditions, the hyperelastic and linear elastic constitutive laws essentially overlap, and configuration changes can be neglected, so that the infinitesimal strain theory remains valid.

As the external load increases, however, the discrepancy between the HE and LE predictions of deformation becomes progressively larger (see Fig. 17b). This arises from both the growing divergence between the constitutive laws and the increasing influence of configuration changes on

the stress and strain measures. Consequently, the two models also exhibit increasingly different predictions of h_{cff} in Fig. 17a. These findings further highlight the importance of employing a nonlinear framework for accurately modeling soft EHL contacts.

In addition to the central film thickness under the fully flooded condition, the frictional behavior between contact surfaces is also a key aspect of tribological studies. In EHL contacts, the frictional force arises from the shear stress $\bar{\boldsymbol{t}}_s^i$ exerted by the fluid on the solid surface Γ_{lt}^i ($i = 1$ for the plate, $i = 2$ for the hemisphere), as defined in Eq. (19). Accordingly, the COF on both contact surfaces is determined as

$$\mu^i = \frac{\left|\int_{\Gamma_{lt}^i} \bar{\boldsymbol{t}}_s^i \cdot \boldsymbol{e_1}\, \mathrm{d}\Gamma\right|}{F/2}. \tag{48}$$

De Vicente et al. [43] also used their linear model to calculate μ^i on both contact surfaces under various operating conditions. Similar to Eq. (47), they derived the following regression equation to predict the COF:

$$\mu^i = \mathrm{SRR}(3.8\,\bar{U}^{0.71}\bar{W}^{-0.76} + 0.96\,\bar{U}^{0.36}\bar{W}^{-0.11}) \pm 1.46\,\bar{U}^{0.65}\bar{W}^{-0.7}, \tag{49}$$

where the slide-to-roll ratio (SRR) is set to 2 for the pure sliding case. The sign of the second term is positive for the plane and negative for the hemisphere. It should be mentioned that their model employs the half-space method to calculate the linear deformation of the gap height. Consequently, the integration domain for their COF calculations is not Γ_{lt}^i, as defined in Eq. (48), but rather the fluid domain Ω_f. In this example, since the lower contact surface is a flat plane, Γ_{lt}^1 can be considered equivalent to Ω_f. However, the upper contact surface, being a curved hemisphere, introduces curvature and deformation effects that are not captured in Eq. (49).

Fig. 18a compares the COF μ^1 on the rigid plane side calculated using the NURBS-based hyperelastic model and Eq. (49) under various external loads and entraining velocities. While the central film thickness predicted by de Vicente et al. [43] differs significantly from the NURBS-based

model at high entraining velocities (see Fig. 17a), the COF results on the rigid plane side exhibit minimal differences and remain largely consistent.

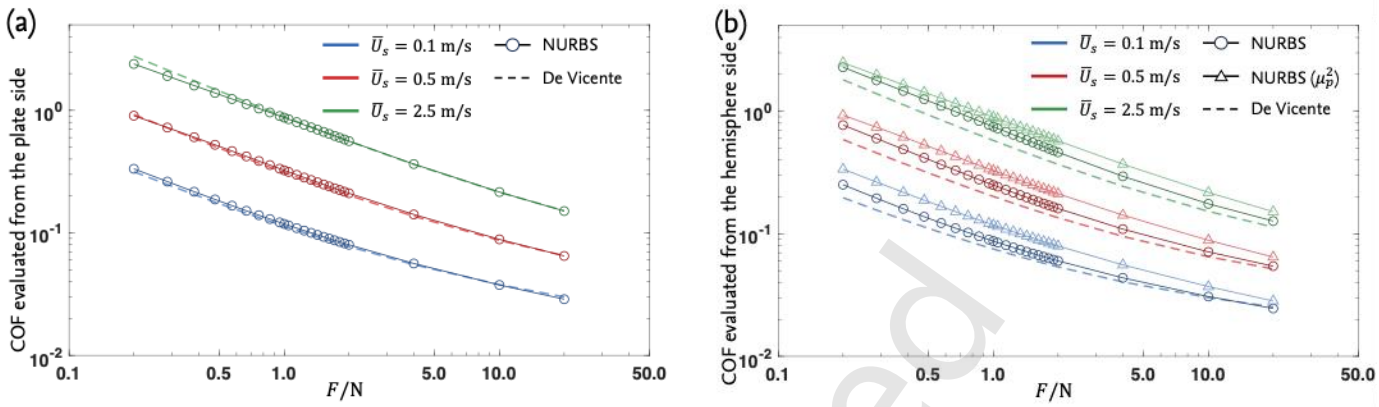

Fig. 18 COF under the fully flooded condition for varying entraining velocities and external loads: (a) COF μ^1 evaluated from the rigid plate side and (b) COF μ^2 evaluated from the hemisphere side. The results of the NURBS-based EHL model are compared with the regression equation Eq. (49) from [43], where μ_p^2 indicates the inclusion of pressure contributions to the frictional force.

Furthermore, Fig. 18b compares the COF μ^2 on the hemisphere side, as computed by both models. Notably, the NURBS-based model utilizes not only Eq. (48) to calculate μ^2, but also an alternative equation, which is denoted as μ_p^2 and defined as

$$\mu_p^2 = \frac{\left|\int_{\Gamma_{It}^i} \left(\bar{\boldsymbol{t}}_s^i - p\bar{\boldsymbol{n}}^2\right) \cdot \boldsymbol{e_1} \, \mathrm{d}\Gamma\right|}{F/2}. \tag{50}$$

The key difference between Eq. (48) and Eq. (50) lies in the inclusion of the x-directional component of fluid pressure in the frictional force calculation, alongside the fluid shear stress.

Fig. 18b demonstrates that when the contribution of fluid pressure is not considered, the μ^2 values calculated using Eq. (49) and the NURBS-based model are largely consistent. As previously mentioned, the small discrepancies between these results stem from the inability of the model proposed by de Vicente et al. [43] to account for geometric changes in the solid contact surfaces caused by large deformations.

However, in practical measurements, the frictional force is generally measured along the sliding direction (e.g., see Sadowski and Stupkiewicz [27]). In this process, it is impossible to distinguish between the contributions of fluid shear stress and fluid pressure. Consequently, the measured frictional force naturally includes the component from fluid pressure, corresponding to μ_p^2 as defined in Eq. (50). Fig. 18b shows that μ_p^2 is notably higher than the estimate provided by Eq. (49), and, as expected, it aligns more closely with μ^1 (see Fig. 18a).

6 Soft EHL contact considering roughness orientation effects

Touche et al. [40] and Baochun et al. [2] experimentally observed that transversely oriented surface roughness enhances lubrication efficiency and reduces friction compared to other orientations. Although Zhu [45] and Baochun et al. [2] have explained this phenomenon using traditional EHL models, their approaches are based on linear elasticity assumptions and infinitesimal deformation theory. To date, no models have investigated whether this conclusion holds for soft materials undergoing nonlinear large deformations.

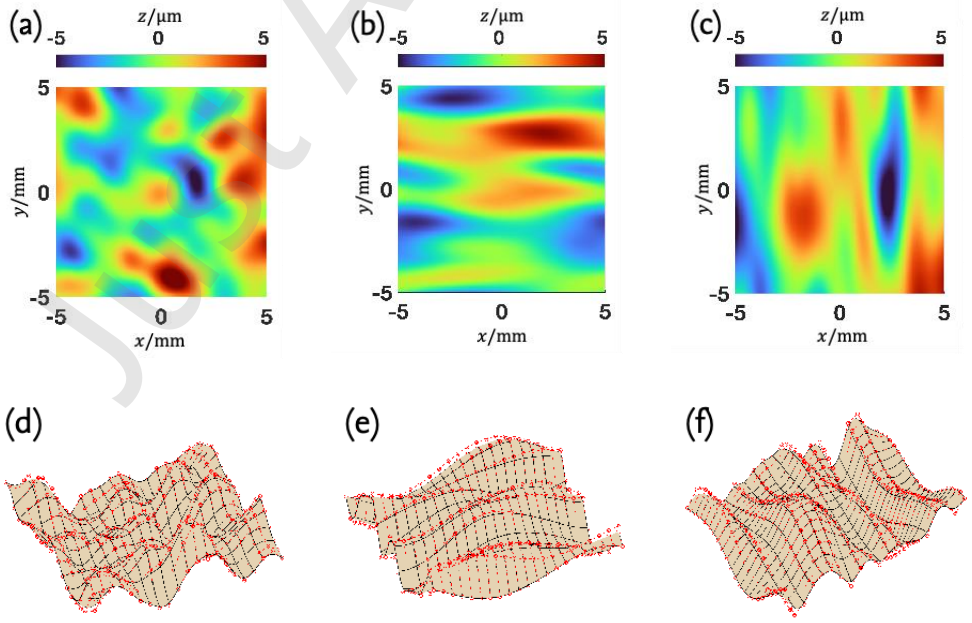

Fig. 19 Randomly generated topographies with (a) isotropic, (b) longitudinal, and (c) transverse roughness orientations, and their corresponding NURBS representations using 21^2 control points (d–f).

In this section, a benchmark example is presented that examines friction between rough surfaces in soft materials, and the newly developed NURBS-based EHL model is employed to solve the problem. Three surfaces with different roughness orientations (see Figs. 19a-c) are generated using the random topography generator developed by Bergström [4]. These topographies are square, with a side length of $L = 10$ mm, and follow the Gaussian distribution. Their root-mean-square (RMS) heights are set to $\sigma = 2$ μm, with the correlation lengths in the x- and y-directions provided below:

$$\text{Isotropic} \Rightarrow l_{cx} = l_{cy} = 1 \text{ mm};$$

$$\text{Longitudinal} \Rightarrow l_{cx} = 2 \text{ mm}, \; l_{cy} = 1 \text{ mm};$$

$$\text{Transverse} \Rightarrow l_{cx} = 1 \text{ mm}, \; l_{cy} = 2 \text{ mm}.$$

The RMS height characterizes the amplitude of the surface roughness, whereas the correlation lengths define the characteristic wavelength of the topographical features and thereby govern the number and spatial distribution of surface peaks and valleys. By prescribing different ratios of correlation lengths in the x- and y-directions while keeping the RMS height fixed, surface roughness orientation is introduced in a controlled manner.

The isotropic topography is taken as a reference configuration, for which equal correlation lengths $l_{cx} = l_{cy} = 1$ mm are selected to generate a sufficiently rich roughness pattern over the surface domain of $L = 10$ mm, while maintaining a computationally feasible mesh resolution. Based on this isotropic reference, longitudinal and transverse roughness orientations are obtained by increasing the correlation length along the x- or y-direction, respectively.

These rough surfaces can be constructed using the NURBS parameterization (the numerical implementation is described in Tong et al. [38]). Due to the high continuity and superior performance of NURBS in handling complex geometries, only 21^2 control points are required to build these three surfaces, as illustrated in Figs. 19d-f.

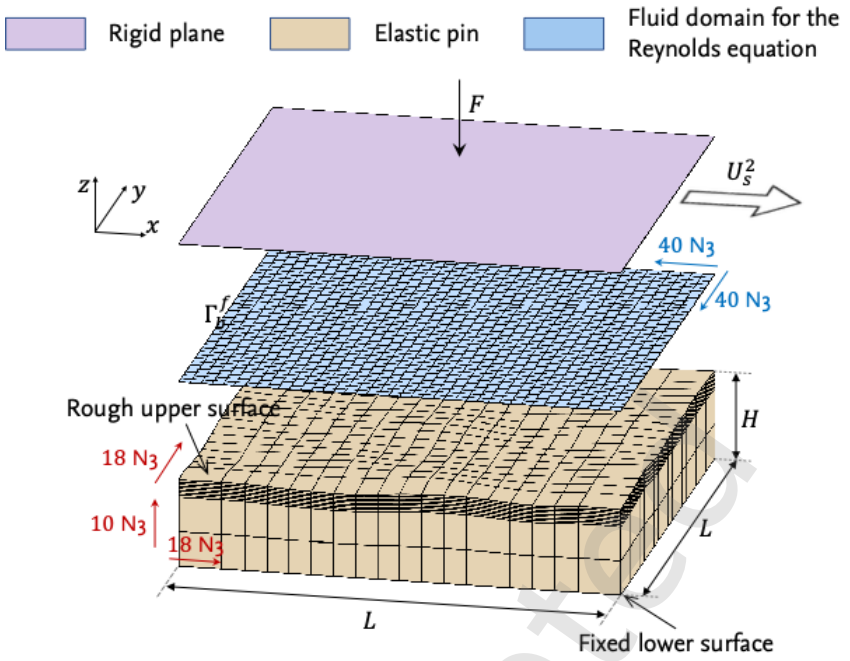

Fig. 20 Soft EHL contact between a rigid plane and an elastic pin with the upper surface configurable to isotropic, longitudinal or transverse roughness patterns.

In this section, the EHL contact between an elastic pin and a rigid plane is investigated (see Fig. 20). The pin has a height of $H = 0.1$ mm, with its lower surface fixed, while its upper surface can be configured using the rough surfaces shown in Fig. 19 to incorporate different topography orientations. The NURBS mesh of the elastic pin is refined with $18 \times 18 \times 10 = 3240$ third-order ($N3$) elements, with local refinement applied near the contact surface. Meanwhile, the fluid mesh is refined with $40 \times 40 = 1600$ $N3$ elements. Further refinement of both solid and fluid meshes resulted only in minor variations of the friction response, confirming that the reported results are essentially mesh-independent.

The rigid plane is pressed downward by an external force F and subject to a prescribed velocity of $U_s^2 = 2$ m/s in the x-direction. The fully flooded condition is considered in this study. Accordingly, the pressure and void fraction at the boundary Γ_b^f of the fluid domain are set as

$$p_b = 0\ Pa, \quad r_b = 0, \quad \forall x_f \in \Gamma_b^f. \tag{51}$$

The pin material is assumed to be hyperelastic, with its constitutive equation defined in Eq. (45). Additionally, the lubricant is considered isoviscous, with a viscosity of $\eta = 0.78$ Pa · s. A summary of the material parameters and boundary conditions is provided in Table 6.

Table 6 Material properties and boundary conditions for the EHL contact considering roughness orientations

Parameter	Value
Pin elastic modulus	$E_s = 2.4$ MPa
Pin poisson's ratio	$\nu_s = 0.49$
Lubricant viscosity	$\eta = 0.78$ Pa · s
Boundary pressure	$p_b = 0$ Pa
Boundary void fraction	$r_b = 0$
Entraining velocity	$\bar{U}_s = 1$ m/s

In this example, the external load F ranges from 0.1 to 12 N. For each value of F, the proposed NURBS-based EHL model is used to compute the stationary result. Subsequently, Eq. (48) can be employed to determine the COF values between the rigid plane and rough surfaces with different topography orientations.

Notably, this section evaluates only the COF μ^2 on the rigid plane, as presented in Fig. 21. This is because the RMS height of the rough surfaces shown in Fig. 19 is extremely small compared to their side lengths, allowing the curvature effects to be neglected. As a result, the COF values computed using Eqs. (48) and (50) for μ^1, μ^2, and μ_p^2 are nearly identical.

The COF curves in Fig. 21 resemble the classical Stribeck curve typically observed in hard EHL contacts [11]. When F is small, the system remains in the hydrodynamic regime, where the gap height is much larger than the RMS roughness, and the influence of topography orientation is negligible, resulting in nearly overlapping COF values. With increasing F, the curves deviate from their initially linear trend, producing a rapid growth in COF.

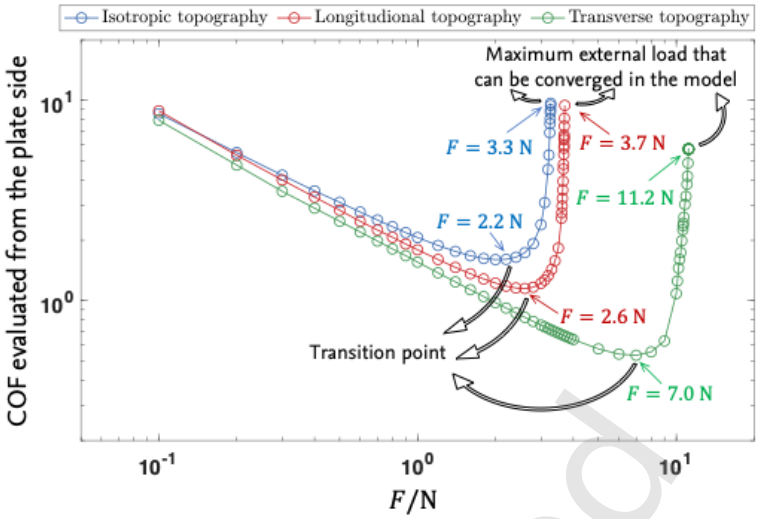

Fig. 21 COF μ^2 evaluated on the rigid plane for different roughness patterns and external loads under the fully flooded condition.

In hard EHL studies, such a sharp COF increase is usually associated with the onset of mixed lubrication, which is conventionally defined as the moment when the first asperity contacts occur (see Spikes [31]). However, this definition is inherently ambiguous, since the precise location and timing of the first asperity contact are difficult to determine in practice. Moreover, the NURBS-based model developed in this work does not incorporate solid contact. For these reasons, we adopt the alternative criterion proposed by Touche et al. [40], where the transition is identified as the point at which the friction coefficient deviates from viscous scaling. Following this definition, the transition points correspond to the minima of the COF curves in Fig. 21, occurring at external loads of 2.2 N, 2.6 N, and 7.0 N for the isotropic, longitudinal, and transverse topographies, respectively.

Table 7 Transition loads, maximum converged loads, and friction-reduction ratios for different topography orientations. The reduction ratio is evaluated at the transition load relative to the COF at the smallest external load in Fig. 21 ($F = 0.1$ N).

Topography orientation	**Transition load F_{tran}/N**	**Max. converged load F_{max}/N**	**COF reduction ratio at transition**
Isotropic	2.2	3.3	81.3%
Longitudinal	2.6	3.7	87.1%
Transverse	7.0	11.2	93.3%

To complement the graphical representation, Table 7 summarizes the transition loads and the corresponding friction-reduction ratios extracted from Fig. 21. It is evident that the transverse topography exhibits the greatest friction reduction (over 90%), whereas the isotropic surface shows the smallest reduction ratio. The pressure and void-fraction distributions at the transition points for different topographies are further illustrated in Fig. 22, while Figs. 23a–c show the corresponding deformed gap-height distributions.

From Fig. 22, it can be observed that the isotropic and longitudinal topographies correspond to relatively small transition forces, which in turn result in lower fluid pressures. Due to the characteristic grooves in the longitudinal topography, pressure tends to build up more easily, leading to a larger non-zero pressure region compared to the isotropic topography, along with lower maximum pressures and cavitation volume fractions.

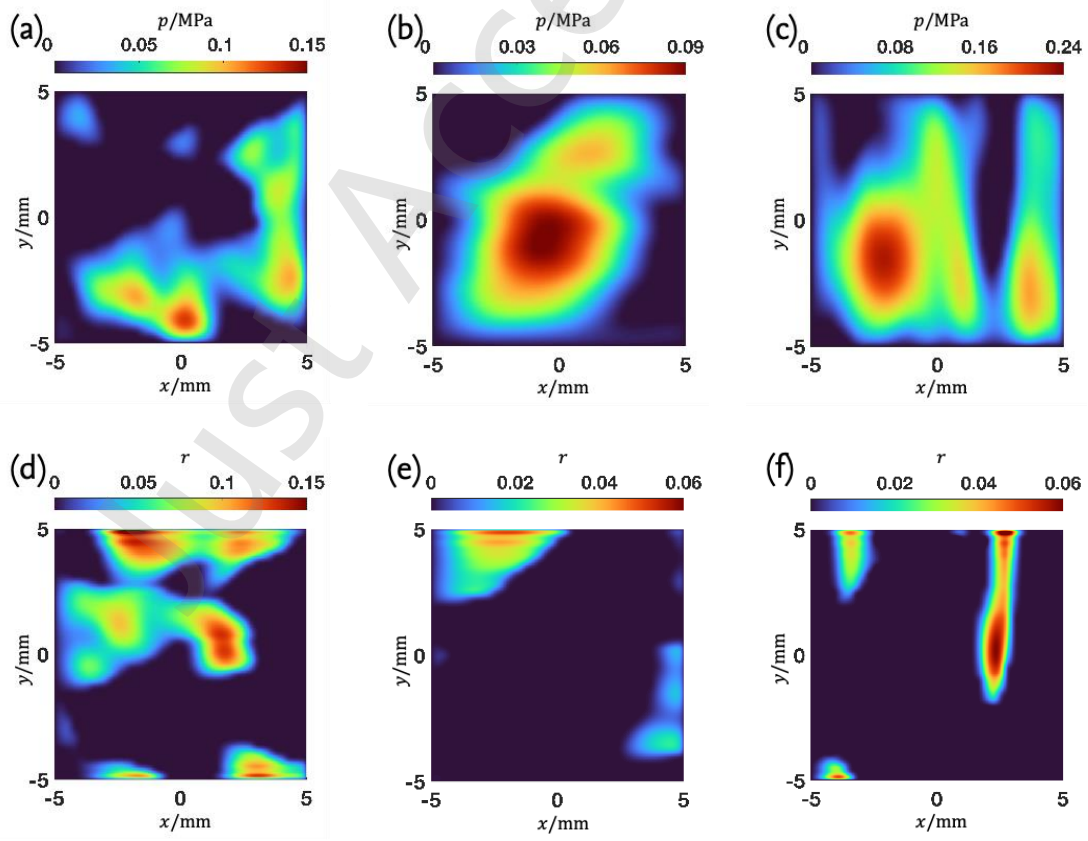

Fig. 22 Pressure p (a–c) and void fraction r (d–f) under the transition external load for different roughness patterns: (a) and (d), isotropic ($F = 2.2$ N); (b) and (e), longitudinal ($F = 2.6$ N); (c) and (f), transverse ($F = 7.0$ N), obtained from the NURBS-based EHL model.

In contrast, the transverse topography exhibits the highest transition force and consequently higher maximum fluid pressures. Furthermore, Figs. 23a-b indicate that at the transition point, the deformed gap height for the isotropic and longitudinal topographies is relatively large, implying that the rough surfaces undergo smaller deformations. Conversely, the transverse topography shows a significantly thinner gap at the transition point (see Fig. 23c), with its profile deviating markedly from the initial undeformed topography shown in Fig. 19c.

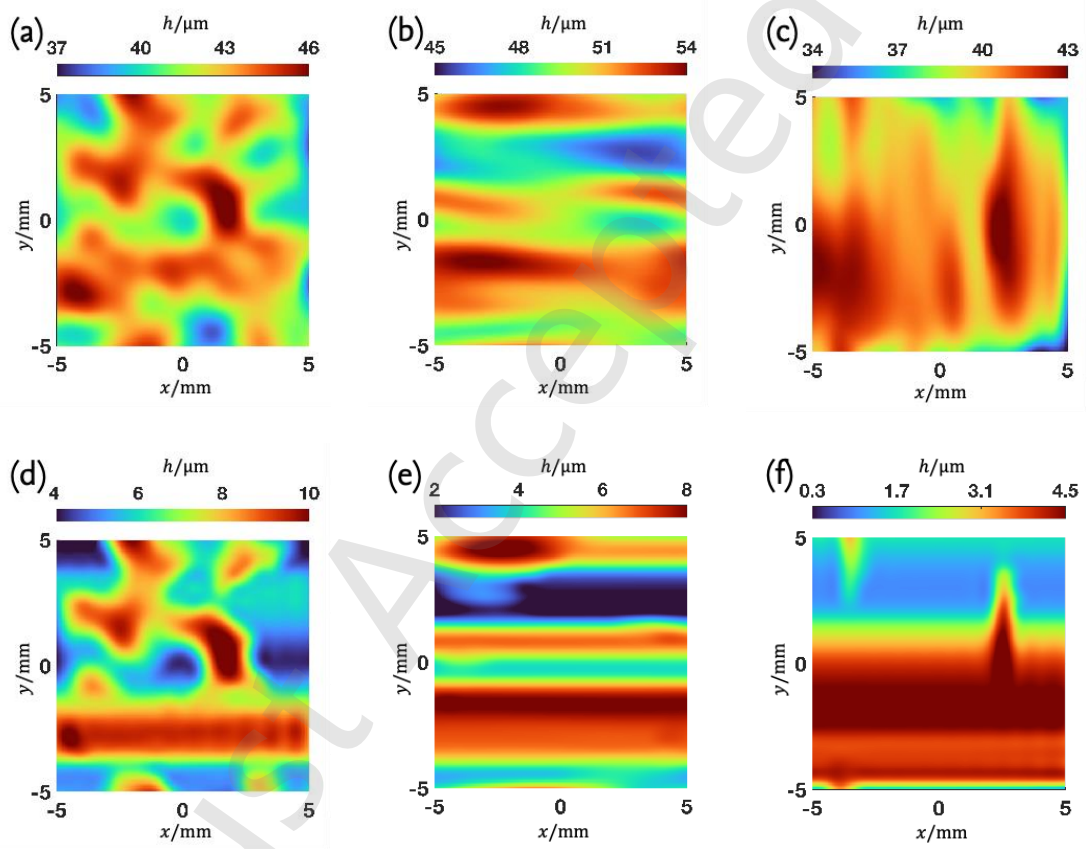

Fig. 23 Deformed gap height h for different roughness patterns under the transition and maximum converged external loads: (a) $F = 2.2$ N, (d) $F = 3.3$ N, isotropic; (b) $F = 2.6$ N, (e) $F = 3.7$ N, longitudinal; (c) $F = 7.0$ N, (f) $F = 11.2$ N, transverse, obtained from the NURBS-based EHL model.

Since solid contact is not considered in the NURBS-based EHL model, it fails to converge when the external load increases beyond a certain limit (see Fig. 21 and Table 7). This maximum convergent force can be interpreted as the upper limit of external load at which no solid contact

occurs in the system. For the isotropic, longitudinal, and transverse topographies, the limit force is 3.3 N, 3.7 N, and 11.2 N, respectively.

Figs. 23d-f show the deformed gap height distributions for the three oriented topographies at the maximum external load. Compared with the corresponding transition states (Figs. 23a-c), the gap height is significantly reduced. Remarkably, irrespective of the orientation, elongated microchannels aligned with the sliding direction (x-direction) are formed adjacent to the minimum gap regions. These channels result from lateral fluid squeezing, which induces surface deformations that transform localized asperity-scale load-bearing regions into extended contact areas. In this way, the microchannels effectively enlarge the pressure-bearing zone, allowing the fluid to sustain higher external loads without the onset of solid contact.

Among the three orientations, the channel associated with the transverse topography is clearly the widest, implying the largest effective pressure-bearing area. This explains why the transverse case sustains the highest load and exhibits the lowest friction. Furthermore, as the external load continues to increase, the microchannels are progressively compressed, leading to the rapid growth of COF observed in Fig. 21. This mechanism differs fundamentally from hard EHL contacts, where the lack of solid compliance precludes the formation of such extended channels and asperity contact occurs directly once the local fluid capacity is exceeded. These findings are consistent with the conclusion of Touche et al. [40], who reported that transverse topographies exhibit superior lubrication efficiency.

7 Conclusions

This work aims to explore tribological phenomena within the EHL regime by developing a comprehensive model based on the NURBS-based IGA framework. The model systematically incorporates the kinematics and tractions involved in EHL contacts, facilitating the consistent linearization of the weak formulation that governs interactions between nonlinear solid deformations and fluid stresses. To discretize the interaction interface, the mortar method is employed, providing

flexibility in mesh sizes and polynomial orders for both fluid and solid domains. This approach substantially reduces computational costs for complex problems, especially in cases requiring denser fluid domain meshes to capture the volumetric distribution of cavitation bubbles accurately.

For validation, benchmark tests of two-dimensional hard and soft EHL line contacts are conducted. In both cases, the NURBS-based framework accurately reproduces the key physical responses on the solid and fluid sides, while achieving a substantial reduction in computational cost compared with the commercial ANSYS FSI model.

Subsequently, the new model is applied to an EHL point contact problem between a hyperelastic hemisphere and a rigid plate, accounting for nonlinear material properties and large deformations. For reference, results from a NURBS-based model with linear elasticity and the regression equations of de Vicente et al. [43] are also included. For the central film thickness and solid deformation, the hyperelastic and linearly elastic models yield nearly identical results under small external loads, consistent with the assumptions of infinitesimal strain theory. As the load increases, however, nonlinear effects become more pronounced and the discrepancies between the two models grow. With regard to the friction coefficient, the regression equations surprisingly provide accurate predictions on the rigid plate side across different external loads and entraining velocities. In contrast, for the COF on the hemisphere side, where curvature effects and the contributions from normal pressure become significant, the regression equations are no longer valid and deviate substantially from the numerical results. The NURBS-based EHL model, however, captures these effects accurately.

This work also investigates the influence of topography orientation on frictional behavior in soft EHL contacts. An example is presented in which a rough surface interacts with a rigid plate. Three randomly generated topographies with identical RMS heights and different roughness orientations (isotropic, longitudinal, and transverse) are adopted for the rough surface. The stationary COF values under various external loads are computed. The results reveal a trend similar to that observed in the

experimental findings of Touche et al. [40]: the transverse topography sustains the highest load at the transition point, and the COF between the contact surfaces is lower than that for the other roughness orientations, indicating superior lubrication performance. Furthermore, this work finds that, regardless of topography orientation, when subjected to extremely high external loads (approaching dry contact), the fluid lubricant is expelled laterally from the contact point, causing deformations in the adjacent surfaces and leading to the formation of micro-channels in the sliding direction.

Notably, the present framework relies on several modeling assumptions, which are briefly summarized here. In the solid mechanics formulation, inertial effects are neglected in the momentum balance, such that the deformation is treated as quasi-static, while geometric nonlinearity and nonlinear material behavior are fully retained. In the fluid formulation, the Reynolds equation is solved using a gap height defined as the distance between opposing surfaces along the global normal direction, without explicitly accounting for curvature effects in the gap height definition. The influence of solid inertia and alternative curvature-aware gap formulations on the predicted EHL response constitutes an interesting topic for future studies.

With respect to the lubrication condition, the present study is restricted to the fully flooded regime. In a complementary study [36], the same framework has been applied to investigate the influence of lubricant quantity on frictional behavior within the starved EHL regime. Beyond these two regimes, the model also holds potential for a wide range of applications, from fundamental tribological research to industrial processes. Examples include the design of artificial hip joints (see Tong and Müller [35]), the modeling of wet grinding processes involving heat transfer (see Thunich et al. [34]), and the prediction of adhesive flow under substrate deformation. The numerical methods and algorithms introduced here provide a solid foundation for achieving accurate and efficient solutions across such applications.

Appendix A. Auxiliary vectors for the mortar-based NURBS discretization

The covariant vectors on Γ_{It}^{i} are defined as $\boldsymbol{\tau}_{\alpha}^{i} \coloneqq \boldsymbol{x}_{s,\alpha}^{i}$ $(\alpha = 1, 2)$, where the subscript $(\blacksquare)_{,\alpha}$ represents the partial derivative operator $\partial(\blacksquare)/\partial\xi_{sI}^{i\alpha}$. They can be connected to the contravariant vectors $\tau^{i\alpha}$ $(\alpha = 1, 2)$ through the metric tensor $\boldsymbol{m}^{i}$:

$$\boldsymbol{\tau}_{\alpha}^{i} = \boldsymbol{m}_{\alpha\beta}^{i}\boldsymbol{\tau}^{i\beta} = \left(\boldsymbol{\tau}_{\alpha}^{i} \cdot \boldsymbol{\tau}_{\beta}^{i}\right)\boldsymbol{\tau}^{i\beta}. \tag{A.1}$$

Notably, Einstein notation is employed for the Greek letters in this equation, with repeated indices summed over. This convention will be maintained for all Greek letters throughout the work.

The variation of $\overline{\boldsymbol{x}}_{s}^{i}$ (defined in Eq. (2)) can then be derived through

$$\delta\overline{\boldsymbol{x}}_{s}^{i} = \left(\delta\boldsymbol{x}_{s}^{i}\right)\big|_{\bar{\xi}_{sI}^{i}} + \delta\bar{\xi}_{sI}^{i\alpha}\boldsymbol{x}_{s,\alpha}^{i}\big|_{\bar{\xi}_{sI}^{i}} = \overline{\boldsymbol{w}}_{s}^{i} + \delta\bar{\xi}_{sI}^{i\alpha}\overline{\boldsymbol{\tau}}_{\alpha}^{i}. \tag{A.2}$$

The first part is the variation when the convective coordinates $\left(\bar{\xi}_{sI}^{i1}, \bar{\xi}_{sI}^{i2}\right)$ remain constant, and the other part arises from the variation of the convective coordinates themselves. For simplicity, the first part of the variation is denoted as $\overline{\boldsymbol{w}}_{s}^{i}$. The variation $\delta\bar{\xi}_{sI}^{i\alpha}$ in the second part is computed using

$$\delta\bar{\xi}_{sI}^{i\alpha} = -\bar{H}^{i\alpha\beta}\overline{\boldsymbol{w}}_{s}^{i} \cdot \boldsymbol{e}_{\beta}, \tag{A.3}$$

where $\bar{H}^{i\alpha\beta}$ $(\alpha, \beta = 1, 2)$ are the inverse components of $\bar{H}_{\alpha\beta}^{i} = \boldsymbol{e}_{\alpha} \cdot \overline{\boldsymbol{\tau}}_{\beta}^{i}$. Consequently, those three auxiliary variations introduced in Eq. (23) can be formulated as

$$\delta\bar{x}_{sn}^{i} = \left(\overline{\boldsymbol{w}}_{s}^{i} + \delta\bar{\xi}_{sI}^{i\alpha}\overline{\boldsymbol{\tau}}_{\alpha}^{i}\right) \cdot \overline{\boldsymbol{n}}^{i} = \overline{\boldsymbol{w}}_{s}^{i} \cdot \overline{\boldsymbol{n}}^{i}, \tag{A.4}$$

$$\delta\bar{x}_{ss1}^{i} = \left(\overline{\boldsymbol{w}}_{s}^{i} + \delta\bar{\xi}_{sI}^{i\alpha}\overline{\boldsymbol{\tau}}_{\alpha}^{i}\right) \cdot \boldsymbol{U}_{sd}, \tag{A.5}$$

$$\delta\bar{x}_{ss2}^{i} = \left(\overline{\boldsymbol{w}}_{s}^{i} + \delta\bar{\xi}_{sI}^{i\alpha}\overline{\boldsymbol{\tau}}_{\alpha}^{i}\right) \cdot \nabla p. \tag{A.6}$$

To facilitate the discretization of the interaction virtual work $\delta\Pi_{s,c}^{i}$ in Eq. (23), the following auxiliary vectors are introduced:

$$\boldsymbol{p} = \left[p_1, p_2, \ \ldots, p_{n_f}\right]^{T}, \tag{A.7}$$

$$\boldsymbol{r} = \left[r_1, r_2, \ \ldots, r_{n_f}\right]^{T}, \tag{A.8}$$

$$\boldsymbol{x}^i = \left[\boldsymbol{x}_{s1}^{iT},\ \boldsymbol{x}_{s2}^{iT},\ \ldots,\ \boldsymbol{x}_{sn_s^i}^{iT}\right]^T, \tag{A.9}$$

$$\delta\boldsymbol{x}^i = \left[\delta\boldsymbol{x}_{s1}^{iT},\ \delta\boldsymbol{x}_{s2}^{iT},\ \ldots,\ \delta\boldsymbol{x}_{sn_s^i}^{iT}\right]^T, \tag{A.10}$$

$$\boldsymbol{R}_f = \left[R_{f1},\ R_{f2},\ \ldots,\ R_{fn_f}\right]^T, \tag{A.11}$$

$$\boldsymbol{N}^i = \left[R_{s1}^i(\bar{\boldsymbol{\xi}}_s^i)\bar{\boldsymbol{n}}^{iT},\ R_{s2}^i(\bar{\boldsymbol{\xi}}_s^i)\bar{\boldsymbol{n}}^{iT},\ \ldots,\ R_{sn_s^i}^i(\bar{\boldsymbol{\xi}}_s^i)\bar{\boldsymbol{n}}^{iT}\right]^T, \tag{A.12}$$

$$\boldsymbol{N}_\alpha^i = \left[R_{s1,\alpha}^i(\bar{\boldsymbol{\xi}}_s^i)\bar{\boldsymbol{n}}^{iT},\ R_{s2,\alpha}^i(\bar{\boldsymbol{\xi}}_s^i)\bar{\boldsymbol{n}}^{iT},\ \ldots,\ R_{sn_s^i,\alpha}^i(\bar{\boldsymbol{\xi}}_s^i)\bar{\boldsymbol{n}}^{iT}\right]^T, \tag{A.13}$$

$$\boldsymbol{T}_\alpha^i = \left[R_{s1}^i(\bar{\boldsymbol{\xi}}_s^i)\bar{\boldsymbol{\tau}}_\alpha^{iT},\ R_{s2}^i(\bar{\boldsymbol{\xi}}_s^i)\bar{\boldsymbol{\tau}}_\alpha^{iT},\ \ldots,\ R_{sn_s^i}^i(\bar{\boldsymbol{\xi}}_s^i)\bar{\boldsymbol{\tau}}_\alpha^{iT}\right]^T, \tag{A.14}$$

$$\boldsymbol{E}_\alpha^i = \left[R_{s1}^i(\bar{\boldsymbol{\xi}}_s^i)\boldsymbol{e}_\alpha^T,\ R_{s2}^i(\bar{\boldsymbol{\xi}}_s^i)\boldsymbol{e}_\alpha^T,\ \ldots,\ R_{sn_s^i}^i(\bar{\boldsymbol{\xi}}_s^i)\boldsymbol{e}_\alpha^T\right]^T, \tag{A.15}$$

$$\boldsymbol{C}_u^i = \left[R_{s1}^i(\bar{\boldsymbol{\xi}}_s^i)\boldsymbol{U}_{sd}^T,\ R_{s2}^i(\bar{\boldsymbol{\xi}}_s^i)\boldsymbol{U}_{sd}^T,\ \ldots,\ R_{sn_s^i}^i(\bar{\boldsymbol{\xi}}_s^i)\boldsymbol{U}_{sd}^T\right]^T, \tag{A.16}$$

$$\boldsymbol{C}_p^i = \left[R_{s1}^i(\bar{\boldsymbol{\xi}}_s^i)\nabla p,\ R_{s2}^i(\bar{\boldsymbol{\xi}}_s^i)\nabla p,\ \ldots,\ R_{sn_s^i}^i(\bar{\boldsymbol{\xi}}_s^i)\nabla p\right]^T, \tag{A.17}$$

$$\boldsymbol{D}_1^i = \frac{1}{det\,\bar{\boldsymbol{H}}^i}\left(\bar{H}_{12}^i\boldsymbol{E}_2^i - \bar{H}_{22}^i\boldsymbol{E}_1^i\right),\quad \boldsymbol{D}_2^i = \frac{1}{det\,\bar{\boldsymbol{H}}^i}\left(\bar{H}_{21}^i\boldsymbol{E}_1^i - \bar{H}_{11}^i\boldsymbol{E}_2^i\right), \tag{A.18}$$

Furthermore, in order to project the interaction virtual work onto the fluid domain using the mortar method, several averaged quantities at control point A ($A = 1,\ \ldots,\ n_f$) are introduced, where the NURBS basis functions act as weighting functions:

$$A_A = \int_{\Omega_f} R_{fA}\ \mathrm{d}\Omega, \tag{A.19}$$

$$h_A = \frac{1}{A_A}\int_{\Omega_f} R_{fA}h\ \mathrm{d}\Omega, \tag{A.20}$$

$$\bar{J}_{sfA}^i = \frac{1}{A_A}\int_{\Omega_f} R_{fA}\bar{J}_{sf}^i\ \mathrm{d}\Omega, \tag{A.21}$$

$$\delta\bar{x}_{snA}^i = \frac{1}{A_A}\int_{\Omega_f} R_{fA}\delta\bar{\boldsymbol{x}}_{sn}^i\ \mathrm{d}\Omega, \tag{A.22}$$

$$\delta\bar{x}_{ss1A}^i = \frac{1}{A_A}\int_{\Omega_f} R_{fA}\delta\bar{\boldsymbol{x}}_{ss1}^i\ \mathrm{d}\Omega, \tag{A.23}$$

$$\delta\bar{x}_{ss2A}^{i}=\frac{1}{A_A}\int_{\Omega_f}R_{fA}\delta\bar{\boldsymbol{x}}_{ss2}^{i}\,\mathrm{d}\Omega\,. \tag{A.24}$$

Substituting Eqs. (A.4)-(A.6) into Eqs. (A.22)-(A.24) leads to

$$\delta\bar{x}_{snA}^{i}=\frac{1}{A_A}\delta\boldsymbol{x}^{iT}\int_{\Omega_f}R_{fA}\boldsymbol{N}^{\boldsymbol{i}}\,\mathrm{d}\Omega=\frac{1}{A_A}\delta\boldsymbol{x}^{iT}\boldsymbol{L}_{nA}^{i}, \tag{A.25}$$

$$\delta\bar{x}_{ss1A}^{i}=\frac{1}{A_A}\delta\boldsymbol{x}^{iT}\int_{\Omega_f}R_{fA}\left[\boldsymbol{C}_{\boldsymbol{u}}^{\boldsymbol{i}}+\left(\bar{\boldsymbol{\tau}}_{\alpha}^{i}\cdot\boldsymbol{U}_{\boldsymbol{sd}}\right)\boldsymbol{D}_{\boldsymbol{\alpha}}^{\boldsymbol{i}}\right]\mathrm{d}\Omega=\frac{1}{A_A}\delta\boldsymbol{x}^{iT}\boldsymbol{L}_{uA}^{i}, \tag{A.26}$$

$$\delta\bar{x}_{ss2A}^{i}=\frac{1}{A_A}\delta\boldsymbol{x}^{iT}\int_{\Omega_f}R_{fA}\left[\boldsymbol{C}_{\boldsymbol{p}}^{\boldsymbol{i}}+\left(\bar{\boldsymbol{\tau}}_{\alpha}^{i}\cdot\nabla p\right)\boldsymbol{D}_{\boldsymbol{\alpha}}^{\boldsymbol{i}}\right]\mathrm{d}\Omega=\frac{1}{A_A}\delta\boldsymbol{x}^{iT}\boldsymbol{L}_{pA}^{i}, \tag{A.27}$$

where L_{nA}^{i}, L_{uA}^{i} and L_{pA}^{i} are introduced to simplify the expressions.

Appendix B. Linearization for the interaction virtual work

Eq. (36) evaluates the interaction virtual work $\delta\Pi_{s,c}^{i}$ using the mortar method. Its linearization follows immediately as

$$\begin{aligned}\Delta\delta\Pi_{s,c}^{i}=&\sum_{A=1}^{n_f}\left[\delta\bar{x}_{snA}^{i}p_A+(-1)^{i}\eta\frac{\delta\bar{x}_{ss1A}^{i}}{h_A}+\frac{1}{2}\delta\bar{x}_{ss2A}^{i}h_A\right]\Delta\bar{j}_{sfA}^{i}A_A\\&+\sum_{A=1}^{n_f}\left[\Delta\delta\bar{x}_{snA}^{i}p_A+(-1)^{i}\eta\frac{\Delta\delta\bar{x}_{ss1A}^{i}}{h_A}+\frac{1}{2}\Delta\delta\bar{x}_{ss2A}^{i}h_A\right]\bar{j}_{sfA}^{i}A_A\\&+\sum_{A=1}^{n_f}\left[\delta\bar{x}_{snA}^{i}\Delta p_A-(-1)^{i}\eta\frac{\delta\bar{x}_{ss1A}^{i}}{h_A^{2}}\Delta h_A+\frac{1}{2}\delta\bar{x}_{ss2A}^{i}\Delta h_A\right]\bar{j}_{sfA}^{i}A_A.\end{aligned} \tag{B.1}$$

The projected linearizations at control points are defined as

$$\Delta h_A=\frac{1}{A_A}\int_{\Omega_f}R_{fA}\,\Delta h\,\mathrm{d}\Omega, \tag{B.2}$$

$$\Delta\bar{j}_{sfA}^{i}=\frac{1}{A_A}\int_{\Omega_f}R_{fA}\Delta\bar{j}_{sf}^{i}\,\mathrm{d}\Omega\,, \tag{B.3}$$

$$\Delta\delta\bar{x}_{snA}^{i}=\frac{1}{A_A}\int_{\Omega_f}R_{fA}\Delta\delta\bar{x}_{sn}^{i}\,\mathrm{d}\Omega\,, \tag{B.4}$$

$$\Delta\delta\bar{x}_{ss1A}^{i}=\frac{1}{A_A}\int_{\Omega_f}R_{fA}\Delta\delta\bar{x}_{ss1}^{i}\,\mathrm{d}\Omega\,, \tag{B.5}$$

$$\Delta\delta\bar{x}_{ss2A}^{i}=\frac{1}{A_A}\int_{\Omega_f}R_{fA}\Delta\delta\bar{x}_{ss2}^{i}\,\mathrm{d}\Omega\,. \tag{B.6}$$

The linearized increments of the corresponding quantities can be obtained in a similar way to the derivation of their variations:

$$\Delta h=\left[\left(\Delta\widetilde{\boldsymbol{x}}_s^2+\Delta\bar{\xi}_{sI}^{2\alpha}\bar{\boldsymbol{\tau}}_\alpha^2\right)-\left(\Delta\widetilde{\boldsymbol{x}}_s^1+\Delta\bar{\xi}_{sI}^{1\alpha}\bar{\boldsymbol{\tau}}_\alpha^1\right)\right]\cdot\boldsymbol{e}_3, \tag{B.7}$$

$$\Delta\bar{J}_{sf}^{i}=\frac{1}{\bar{J}_{sf}^{i}}\nabla\bar{z}_s^i\cdot\Delta\left(\nabla\bar{z}_s^i\right), \tag{B.8}$$

$$\Delta\delta\bar{x}_{sn}^{i}=\Delta\bar{\xi}_{sI}^{i\alpha}\bar{\boldsymbol{w}}_{s,\alpha}^{i}\cdot\bar{\boldsymbol{n}}^{i}-\left[\bar{\boldsymbol{n}}^{i}\cdot\left(\Delta\widetilde{\boldsymbol{x}}_{s,\alpha}^{i}+\Delta\bar{\xi}_{sI}^{i\beta}\bar{\boldsymbol{x}}_{s,\alpha\beta}^{i}\right)\right]\left(\bar{\boldsymbol{w}}_s^i\cdot\bar{\boldsymbol{\tau}}^{i\alpha}\right), \tag{B.9}$$

$$\Delta\delta\bar{x}_{ss1}^{i}=\left(\Delta\bar{\boldsymbol{w}}_s^i+\Delta\delta\bar{\xi}_{sI}^{i\alpha}\bar{\boldsymbol{\tau}}_\alpha^i+\delta\bar{\xi}_{sI}^{i\alpha}\Delta\bar{\boldsymbol{\tau}}_\alpha^i\right)\cdot\boldsymbol{U}_{sd}, \tag{B.10}$$

$$\Delta\delta\bar{x}_{ss2}^{i}=\left(\Delta\bar{\boldsymbol{w}}_s^i+\Delta\delta\bar{\xi}_{sI}^{i\alpha}\bar{\boldsymbol{\tau}}_\alpha^i+\delta\bar{\xi}_{sI}^{i\alpha}\Delta\bar{\boldsymbol{\tau}}_\alpha^i\right)\cdot\nabla p+\left(\bar{\boldsymbol{w}}_s^i+\delta\bar{\xi}_{sI}^{i\alpha}\bar{\boldsymbol{\tau}}_\alpha^i\right)\cdot\Delta(\nabla p), \tag{B.11}$$

$$\Delta\delta\bar{\xi}_s^{i\alpha}=-\bar{H}^{i\alpha\beta}\left(\delta\bar{\xi}_{sI}^{i\gamma}\Delta\widetilde{\boldsymbol{x}}_{s,\gamma}^{i}+\delta\bar{\xi}_{sI}^{i\gamma}\bar{\boldsymbol{x}}_{s,\gamma\theta}^{i}\Delta\bar{\xi}_{sI}^{i\theta}+\bar{w}_{s,\gamma}^{i}\Delta\bar{\xi}_{sI}^{i\gamma}\right)\cdot\boldsymbol{e}_\beta. \tag{B.12}$$

Notably, $\Delta\widetilde{\blacksquare}$ is used to signify $(\Delta\blacksquare)|_{\bar{\boldsymbol{\xi}}_s^i}$, to differentiate it from $\Delta\blacksquare$. By introducing the following auxiliary matrices:

$$\boldsymbol{E}_{\alpha,\beta}^{i}=\left[R_{s1,\beta}^{i}\left(\bar{\boldsymbol{\xi}}_s^i\right)\boldsymbol{e}_\alpha^T,\ R_{s2,\beta}^{i}\left(\bar{\boldsymbol{\xi}}_s^i\right)\boldsymbol{e}_\alpha^T,\ \ldots,\ R_{sn_s^i,\beta}^{i}\left(\bar{\boldsymbol{\xi}}_s^i\right)\boldsymbol{e}_\alpha^T\right]^T, \tag{B.13}$$

$$k_{\alpha\beta}^{i}=\bar{\boldsymbol{\tau}}_{\alpha,\beta}^{i}\cdot\bar{\boldsymbol{n}}^{i},\ k_{\beta\gamma\alpha}^{i}=\bar{\boldsymbol{\tau}}_{\beta,\gamma}^{i}\cdot\boldsymbol{e}_\alpha, \tag{B.14}$$

$$\bar{\boldsymbol{N}}_1^i=\boldsymbol{N}_1^i+k_{11}^i\boldsymbol{D}_1^i+k_{12}^i\boldsymbol{D}_2^i,\ \bar{\boldsymbol{N}}_2^i=\boldsymbol{N}_2^i+k_{21}^i\boldsymbol{D}_1^i+k_{22}^i\boldsymbol{D}_2^i, \tag{B.15}$$

$$\bar{\boldsymbol{E}}_\alpha^i=\left[\boldsymbol{E}_{\alpha,1}^i+k_{11\alpha}^i\boldsymbol{D}_1^i+k_{12\alpha}^i\boldsymbol{D}_2^i,\ \boldsymbol{E}_{\alpha,2}^i+k_{21\alpha}^i\boldsymbol{D}_1^i+k_{22\alpha}^i\boldsymbol{D}_2^i\right], \tag{B.16}$$

$$\boldsymbol{C}_{u\alpha}^{i}=\left[R_{s1,\alpha}^{i}\left(\bar{\boldsymbol{\xi}}_s^i\right)\boldsymbol{U}_{sd}^T,\ R_{s2,\alpha}^{i}\left(\bar{\boldsymbol{\xi}}_s^i\right)\boldsymbol{U}_{sd}^T,\ \ldots,\ R_{sn_s^i,\alpha}^{i}\left(\bar{\boldsymbol{\xi}}_s^i\right)\boldsymbol{U}_{sd}^T\right]^T, \tag{B.17}$$

$$\boldsymbol{C}_{p\alpha}^{i}=\left[R_{s1,\alpha}^{i}\left(\bar{\boldsymbol{\xi}}_s^i\right)\nabla p,\ R_{s2,\alpha}^{i}\left(\bar{\boldsymbol{\xi}}_s^i\right)\nabla p,\ \ldots,\ R_{sn_s^i,\alpha}^{i}\left(\bar{\boldsymbol{\xi}}_s^i\right)\nabla p\right]^T, \tag{B.18}$$

$$\boldsymbol{C}_R^i=\left[R_{s1}^{i}\left(\bar{\boldsymbol{\xi}}_s^i\right)\nabla R_f,\ R_{s2}^{i}\left(\bar{\boldsymbol{\xi}}_s^i\right)\nabla R_f,\ \ldots,\ R_{sn_s^i}^{i}\left(\bar{\boldsymbol{\xi}}_s^i\right)\nabla R_f\right]^T, \tag{B.19}$$

$$\boldsymbol{J}^i = \begin{bmatrix} \dfrac{\partial x}{\partial \xi_{sI}^{i1}} & \dfrac{\partial x}{\partial \xi_{sI}^{i2}} \\ \dfrac{\partial y}{\partial \xi_{sI}^{i1}} & \dfrac{\partial y}{\partial \xi_{sI}^{i2}} \end{bmatrix}, \tag{B.20}$$

$$\boldsymbol{C}_z^{iT} = \left(\bar{\boldsymbol{J}}^i\right)^{-T} \overline{\boldsymbol{E}}_3^{iT} - \frac{(\bar{\boldsymbol{J}}^i)^{-T}}{det\,\bar{\boldsymbol{J}}^i}\left(\bar{J}_{22}^i \bar{z}_{s,1}^i - \bar{J}_{21}^i \bar{z}_{s,2}^i\right)\overline{\boldsymbol{E}}_1^{iT} - \frac{\left(\bar{\boldsymbol{J}}^i\right)^{-T}}{det\,\bar{\boldsymbol{J}}^i}\left(\bar{J}_{11}^i \bar{z}_{s,2}^i - \bar{J}_{12}^i \bar{z}_{s,1}^i\right)\overline{\boldsymbol{E}}_2^{iT}, \tag{B.21}$$

$$\boldsymbol{C}_j^{iT} = \frac{1}{\bar{J}_{sf}^i} \nabla \bar{z}_s^i \boldsymbol{C}_z^{iT}, \tag{B.22}$$

$$\boldsymbol{k}_{sn}^i = \boldsymbol{N}_\alpha^i \boldsymbol{D}_\alpha^{iT} - m^{i\alpha\beta} \boldsymbol{T}_\beta^i \overline{\boldsymbol{N}}_\alpha^{iT}, \tag{B.23}$$

$$\boldsymbol{k}_\xi^{i\alpha} = -\bar{H}^{i\alpha\beta}\left(\boldsymbol{E}_{\beta,\gamma}^i \boldsymbol{D}_\gamma^{iT} + \boldsymbol{D}_\gamma^i \boldsymbol{E}_{\beta,\gamma}^{iT} + k_{\gamma\theta\beta}^i \boldsymbol{D}_\gamma^i \boldsymbol{D}_\theta^{iT}\right), \tag{B.24}$$

$$\boldsymbol{k}_{ss1}^i = \boldsymbol{C}_{u\alpha}^i \boldsymbol{D}_\alpha^{iT} + \left(\bar{\boldsymbol{\tau}}_\alpha^i \cdot \boldsymbol{U}_{sd}\right)\boldsymbol{k}_\xi^{i\alpha} + \boldsymbol{D}_\alpha^i \boldsymbol{C}_{u\alpha}^{iT} + \left(\bar{\boldsymbol{x}}_{s,\alpha\beta}^i \cdot \boldsymbol{U}_{sd}\right)\boldsymbol{D}_\alpha^i \boldsymbol{D}_\beta^{iT}, \tag{B.25}$$

$$\boldsymbol{k}_{ss2}^{ix} = \boldsymbol{C}_{p\alpha}^i \boldsymbol{D}_\alpha^{iT} + \left(\bar{\boldsymbol{\tau}}_\alpha^i \cdot \nabla p\right)\boldsymbol{k}_\xi^{i\alpha} + \boldsymbol{D}_\alpha^i \boldsymbol{C}_{p\alpha}^{iT} + \left(\bar{\boldsymbol{x}}_{s,\alpha\beta}^i \cdot \nabla p\right)\boldsymbol{D}_\alpha^i \boldsymbol{D}_\beta^{iT}, \tag{B.26}$$

$$\boldsymbol{k}_{ss2}^{ip} = \boldsymbol{C}_R^i + \boldsymbol{D}_\alpha^i \bar{\boldsymbol{\tau}}_\alpha^{iT}\left(\nabla R_f\right)^T, \tag{B.27}$$

the linearized quantities in Eqs. (B.7)-(B.12) can be recast in matrix form:

$$\Delta h = \sum_{i=1}^{2} (-1)^i \left[\boldsymbol{E}_3^{iT} + \left(\bar{\boldsymbol{\tau}}_\alpha^i \cdot \boldsymbol{e}_3\right)\boldsymbol{D}_\alpha^{iT}\right]\Delta \boldsymbol{x}^i, \tag{B.28}$$

$$\Delta \bar{J}_{sf}^i = \boldsymbol{C}_j^{iT} \Delta \boldsymbol{x}^i, \tag{B.29}$$

$$\Delta \delta \bar{x}_{sn}^i = \delta \boldsymbol{x}^{iT} \boldsymbol{k}_{sn}^i \Delta \boldsymbol{x}^i, \tag{B.30}$$

$$\Delta \delta \bar{x}_{ss1}^i = \delta \boldsymbol{x}^{iT} \boldsymbol{k}_{ss1}^i \Delta \boldsymbol{x}^i, \tag{B.31}$$

$$\Delta \delta \bar{x}_{ss2}^i = \delta \boldsymbol{x}^{iT} \boldsymbol{k}_{ss2}^{ix} \Delta \boldsymbol{x}^i + \delta \boldsymbol{x}^{iT} \boldsymbol{k}_{ss2}^{ip} \Delta p. \tag{B.32}$$

Finally, substituting all the variational and linearized quantities, whose matrix forms are derived in this appendix as well as in Sec. 3.2, into Eq. (B.1) results in

$$\Delta \delta \Pi_{slh}^i = \delta \boldsymbol{x}^{iT} \boldsymbol{J}_{xx}^{il} \Delta \boldsymbol{x}^i + \delta \boldsymbol{x}^{iT} \boldsymbol{J}_{xx}^{ijl} \Delta \boldsymbol{x}^i + \delta \boldsymbol{x}^{iT} \boldsymbol{J}_{xp}^{il} \Delta \boldsymbol{p}, \qquad j \neq i. \tag{B.33}$$

The Jacobian matrices, required for the iterative solution using the Newton-Raphson method, are computed through

$$\boldsymbol{J}_{xx}^{iI} = \sum_{A=1}^{n_f}\left[p_A\boldsymbol{L}_{nA}^{i}\boldsymbol{L}_{jA}^{iT} + (-1)^i\frac{\eta}{h_A}\boldsymbol{L}_{uA}^{i}\boldsymbol{L}_{jA}^{iT} + \frac{1}{2}h_A\boldsymbol{L}_{pA}^{i}\boldsymbol{L}_{jA}^{iT}\right] + \int_{\Omega_f}\sum_{A=1}^{n_f}\left(R_{fA}p_A\bar{J}_{sfA}^{i}\right)\boldsymbol{k}_{\boldsymbol{sn}}^{\boldsymbol{i}}\,d\Omega \qquad (B.34)$$

$$+(-1)^i\eta\int_{\Omega_f}\sum_{A=1}^{n_f}\left(R_{fA}\frac{\bar{J}_{sfA}^{i}}{h_A}\right)\boldsymbol{k}_{ss1}^{i}\,d\Omega + \frac{1}{2}\int_{\Omega_f}\sum_{A=1}^{n_f}\left(R_{fA}h_A\bar{J}_{sfA}^{i}\right)\boldsymbol{k}_{ss2}^{ix}\,\mathrm{d}\Omega$$

$$+\sum_{A=1}^{n_f}\left[(-1)^{i+1}\eta\frac{\bar{J}_{sfA}^{i}}{h_A^2}\boldsymbol{L}_{uA}^{i}\boldsymbol{L}_{hA}^{iT} + \frac{1}{2}\bar{J}_{sfA}^{i}\boldsymbol{L}_{pA}^{i}\boldsymbol{L}_{hA}^{iT}\right],$$

$$\boldsymbol{J}_{xx}^{ijI} = \sum_{A=1}^{n_f}\left[(-1)^{i+1}\eta\frac{\bar{J}_{sfA}^{i}}{h_A^2}\boldsymbol{L}_{uA}^{i}\boldsymbol{L}_{hA}^{jT} + \frac{1}{2}\bar{J}_{sfA}^{i}\boldsymbol{L}_{pA}^{i}\boldsymbol{L}_{hA}^{jT}\right], \qquad (B.35)$$

$$\boldsymbol{J}_{xp}^{iI} = \frac{1}{2}\int_{\Omega_f}\sum_{A=1}^{n_f}\left(R_{fA}h_A\bar{J}_{sfA}^{i}\right)\boldsymbol{k}_{ss2}^{ip}\,\mathrm{d}\Omega + \left[\boldsymbol{L}_{n1}^{i}\bar{J}_{sf1}^{i},\ \boldsymbol{L}_{n2}^{i}\bar{J}_{sf2}^{i},\ \ldots,\ \boldsymbol{L}_{nn_f}^{i}\bar{J}_{sfn_f}^{i}\right]. \qquad (B.36)$$

with

$$\boldsymbol{L}_{hA}^{i} = \frac{(-1)^i}{A_A}\int_{\Omega_f}R_{fA}\left[\boldsymbol{E}_3^{i} + \left(\bar{\boldsymbol{\tau}}_{\alpha}^{i}\cdot\boldsymbol{e}_3\right)\boldsymbol{D}_{\alpha}^{i}\right]\mathrm{d}\Omega, \qquad (B.37)$$

$$\boldsymbol{L}_{jA}^{i} = \frac{1}{A_A}\int_{\Omega_f}R_{fA}\boldsymbol{C}_j^{i}\,\mathrm{d}\Omega. \qquad (B.38)$$

References

[1] Allen Q, Raeymaekers B. Soft EHL Simulations of Lubricant Film Thickness in Textured Hard-on-Soft Bearings Considering Different Cavitation Models, in the Context of Prosthetic Hip Implants. *Tribol Lett* **69**(4): 118 (2021)

[2] Baochun C, Huazhen J, Wenzhong W, Zhengyang L, Baoan W, Bing Y, Zhiyuan R. Influence of surface roughness orientations on friction coefficient of wheel/rail specimen in oil lubrication. *Chinese Journal of Theoretical and Applied Mechanics* **48**(5): 1114–1125 (2016)

[3] Bartel D. *Simulation von Tribosystemen*. Vieweg+Teubner, 2010.

[4] Bergström D. MySimLabs. Information on http://www.mysimlabs.com/index.html

[5] Braun MJ, Hannon WM. Cavitation formation and modelling for fluid film bearings: A review. *Proceedings of the Institution of Mechanical Engineers, Part J: Journal of Engineering Tribology* **224**(9): 839–863 (2010)

[6] Brooks AN, Hughes TJR. Streamline upwind/Petrov-Galerkin formulations for convection dominated flows with particular emphasis on the incompressible Navier-Stokes equations. *Comput Methods Appl Mech Eng* **32**(1): 199–259 (1982)

[7] Cottrell JA, Hughes TJR, Bazilevs Y. *Isogeometric analysis: toward integration of CAD and FEA*. John Wiley & Sons, 2009.

[8] Faraji M, Seitz A, Meier C, Wall WA. A Mortar Finite Element Formulation for Large Deformation Lubricated Contact Problems with Smooth Transition Between Mixed, Elasto-Hydrodynamic and Full Hydrodynamic Lubrication. *Tribol Lett* **71**(1): 11 (2022)

[9] Habchi W, Eyheramendy D, Vergne P, Morales-Espejel G. Stabilized fully-coupled finite elements for elastohydrodynamic lubrication problems. *Advances in Engineering Software* **46**(1): 4–18 (2012)

[10] Hamrock BJ, Dowson D. Isothermal Elastohydrodynamic Lubrication of Point Contacts: Part 1Theoretical Formulation. *Journal of Lubrication Technology* **98**(2): 223–228 (1976)

[11] Hamrock BJ, Schmid SR, Jacobson BO. *Fundamentals of Fluid Film Lubrication*. CRC Press, 2004.

[12] Hansen E, Kacan A, Frohnapfel B, Codrignani A. An EHL Extension of the Unsteady FBNS Algorithm. *Tribol Lett* **70**(3): 80 (2022)

[13] Holmes MJA, Evans HP, Hughes TG, Snidle RW. Transient elastohydrodynamic point contact analysis using a new coupled differential deflection method Part 1: Theory and validation. *Proceedings of the Institution of Mechanical Engineers, Part J: Journal of Engineering Tribology* **217**(4): 289–304 (2003)

[14] Hsiao H-SS, Hamrock BJ, Tripp JH. Finite Element System Approach to EHL of Elliptical Contacts: Part IIsothermal Circular Non-Newtonian Formulation. *J Tribol* **120**(4): 695–704 (1998)

[15] Hughes TJR, Cottrell JA, Bazilevs Y. Isogeometric analysis: CAD, finite elements, NURBS, exact geometry and mesh refinement. *Comput Methods Appl Mech Eng* **194**(39): 4135–4195 (2005)

[16] Hughes TJR, Franca LP, Hulbert GM. A new finite element formulation for computational fluid dynamics: VIII. The galerkin/least-squares method for advective-diffusive equations. *Comput Methods Appl Mech Eng* **73**(2): 173–189 (1989)

[17] Jiang S, Liu Q, Ji H, Wang W, Meng Z, Wang J, Dong G. Modeling and analysis for surface texturing on soft sliders in mixed lubrication. *Friction* **13**(3): 9440917 (2025)

[18] Johnson KL. *Contact Mechanics*. Cambridge University Press, 1985.

[19] Liu S, Wang Q, Liu G. A versatile method of discrete convolution and FFT (DC-FFT) for contact analyses. *Wear* **243**(1–2): 101–111 (2000)

[20] De Lorenzis L, Temizer İ, Wriggers P, Zavarise G. A large deformation frictional contact formulation using NURBS-based isogeometric analysis. *Int J Numer Methods Eng* **87**(13): 1278–1300 (2011)

[21] De Lorenzis L, Wriggers P, Zavarise G. A mortar formulation for 3D large deformation contact using NURBS-based isogeometric analysis and the augmented Lagrangian method. *Comput Mech* **49**(1): 1–20 (2011)

[22] Lubrecht AA, ten Napel WE, Bosma R. Multigrid, an Alternative Method of Solution for Two-Dimensional Elastohydrodynamically Lubricated Point Contact Calculations. *J Tribol* **109**(3): 437–443 (1987)

[23] Lugt PM, Morales-Espejel GE. A Review of Elasto-Hydrodynamic Lubrication Theory. *Tribology Transactions* **54**(3): 470–496 (2011)

[24] Piegl L, Tiller W. *The NURBS Book*. Springer Berlin Heidelberg, 1995.

[25] Popov VL. Rigorous Treatment of Contact Problems – Hertzian Contact. In: *Contact Mechanics and Friction*, Springer Berlin Heidelberg, 2010, 55–70.

[26] Popp A, Wall WA. Dual mortar methods for computational contact mechanics. *GAMM-Mitteilungen* **37**(1): 66–84 (2014)

[27] Sadowski P, Stupkiewicz S. Friction in lubricated soft-on-hard, hard-on-soft and soft-on-soft sliding contacts. *Tribol Int* **129**: 246–256 (2019)

[28] Shen D, Salant RF. An unsteady mixed soft EHL model, with application to a rotary lip seal. *Tribol Int* **40**(4): 646–651 (2007)

[29] Shinkarenko A, Kligerman Y, Etsion I. The effect of surface texturing in soft elasto-hydrodynamic lubrication. *Tribol Int* **42**(2): 284–292 (2009)

[30] Singh K, Sadeghi F, Russell T, Lorenz SJ, Peterson W, Villarreal J, Jinmon T. Fluid–Structure Interaction Modeling of Elastohydrodynamically Lubricated Line Contacts. *J Tribol* **143**(9): 91602 (2021)

[31] Spikes HA. Mixed lubrication — an overview. *Lubrication Science* **9**(3): 221–253 (1997)

[32] Stupkiewicz S, Lengiewicz J, Sadowski P, Kucharski S. Finite deformation effects in soft elastohydrodynamic lubrication problems. *Tribol Int* **93**: 511–522 (2016)

[33] Temizer İ, Stupkiewicz S. Formulation of the Reynolds equation on a time-dependent lubrication surface. *Proceedings of the Royal Society A: Mathematical, Physical and Engineering Sciences* **472**(2187): 20160032 (2016)

[34] Thunich P, Tong Y, Müller M. Efficient modelling of thermo-hydrodynamic properties in lubricated technical systems using NURBS-based isogeometric analysis. *Tribol Int* 109934 (2024)

[35] Tong Y, Müller M. An Elastohydrodynamic Lubrication Framework for Hip Prostheses based on Isogeometric Analysis. (2024)

[36] Tong Y, Müller M. Investigation of starved soft EHL contacts using NURBS-based isogeometric analysis. *Tribol Int* **212**: 110965 (2025)

[37] Tong Y, Müller M, Ostermeyer G-P. Investigations on the dynamic influence of the contact angle on frictional sliding processes between rough surfaces using NURBS and mortar-based augmented Lagrangian method. *Tribol Int* **158**: 106889 (2021)

[38] Tong Y, Müller M, Ostermeyer G-P. A mortar-based cavitation formulation using NURBS-based isogeometric analysis. *Comput Methods Appl Mech Eng* **398**: 115263 (2022)

[39] Tong Y, Müller M, Ostermeyer G-P. An arbitrary Lagrangian–Eulerian formulation for the Reynolds equation considering the JFO boundary condition. *PAMM* **23**(3): e202300216 (2023)

[40] Touche T, Cayer-Barrioz J, Mazuyer D. Friction of Textured Surfaces in EHL and Mixed Lubrication: Effect of the Groove Topography. *Tribol Lett* **63**(2): 25 (2016)

[41] Tur M, Fuenmayor FJ, Wriggers P. A mortar-based frictional contact formulation for large deformations using Lagrange multipliers. *Comput Methods Appl Mech Eng* **198**(37): 2860–2873 (2009)

[42] Venner CH. Multilevel solution of the EHL line and point contact problems. Ph.D. Thesis, Netherlands, 1991.

[43] de Vicente J, Stokes JR, Spikes HA. The Frictional Properties of Newtonian Fluids in Rolling–Sliding soft-EHL Contact. *Tribol Lett* **20**(3): 273–286 (2005)

[44] Wriggers P. *Nonlinear Finite Element Methods*. Springer Berlin Heidelberg, 2008.

[45] Zhu D. Effect of Surface Roughness on Mixed EHD Lubrication Characteristics. *Tribology Transactions* **46**(1): 44–48 (2003)